

DESIGN OF A MICROWAVE LENS FOR 5G APPLICATIONS

by
MEHMET BORA ÖZDEMİR

Submitted to the Graduate School of Engineering and Natural Sciences
in partial fulfilment of
the requirements for the degree of Master of Science

Sabancı University
July 2022

MEHMET BORA ÖZDEMİR 2022 ©

All Rights Reserved

ABSTRACT

DESIGN OF A MICROWAVE LENS FOR 5G APPLICATIONS

MEHMET BORA ÖZDEMİR

Electronics Engineering MSc. Thesis, July 2022

Thesis Advisor: Prof. İbrahim Tekin

Keywords: Rotman Lens, multilayer, 5G communications, beam-steering, millimeter-wave, microstrip lens, beam forming network, 28GHz

This thesis proposes a novel, low-cost, multilayer Rotman lens and antenna array for 5G applications at 28GHz band. The final design consists of a multilayered Rotman Lens, with the antenna array on the front and the Rotman Lens on the backside of the board. The lens and array are connected by slots opened to the common ground layer that is between them. This two layered structure made it possible to reduce the total footprint of the design. These slots were designed so that the insertion loss through them is less than 1dB. The design of the dummy ports found on the sides of the Rotman Lens was also changed. The dummy ports require 50Ω terminations to reduce the reflections occurring on the sidewalls to prevent unwanted phase shifts. The dummy ports were terminated using quarter wave transformation techniques. Using the quarter wave transformations, the dummy ports were matched to 200Ω . These transmission lines were paired in two so that they are each matched to 100Ω and require 100Ω terminations to These connections were done so that they act as terminations to each other. These connections made it possible to remove the 50Ω connectors necessary to reduce the sidewall reflections. This way, the size and cost of the design was lowered further. Conventional Rotman Lens designs can produce beams equal to the number of beam ports it has. The feeding network of the lens was designed using in-phase transmission lines, allowing multiple inputs to be fed together to generate two extra beams. The measured beams have gains between 9.2 and 13.7dBi. The beams cover an area of 80° , with a 3dB bandwidth of 2GHz.

ÖZET

5G UYGULAMALARI İÇİN MİKRODALGA LENS TASARIMI

MEHMET BORA ÖZDEMİR

Elektronik Mühendisliği Yüksek Lisans Tezi, Temmuz 2022

Tez Danışmanı: Prof. İbrahim Tekin

Anahtar Kelimeler: Rotman Lens, çok katmanlı, 5G iletişim, ışın yönlendirme, milimetre dalga, mikroserit lens, ışın oluşturma ağı, 28GHz

Bu tez, 28 GHz bandında 5G uygulamaları için yeni, düşük maliyetli, çok katmanlı bir Rotman lens ve anten dizisi önermektedir. Nihai tasarım, önde anten dizisi ve arka tarafta Rotman Lens olmak üzere iki katmanlı bir karttan oluşur. Lens ve dizinin bağlantısı, aralarındaki ortak toprak katmanına açılan yuvalarla sağlanmıştır. Bu iki katmanlı yapı, tasarımın toplam ayak izini azaltmayı mümkün kılmıştır. Bu yuvalar üzerlerindeki güç kaybı 1dB'den az olacak şekilde tasarlanmıştır. Rotman Lens'in yan taraflarında bulunan sahte bağlantıların tasarımında da değişiklik yapıldı. Sahte bağlantı noktaları, istenmeyen faz kaymalarını önlemek üzere yan duvarlarda meydana gelen yansımaları azaltmak için 50Ω sonlandırmaları gerektirir. Sahte bağlantı noktaları, çeyrek dalga dönüşüm teknikleri kullanılarak sonlandırıldı. Çeyrek dalga dönüşümleri kullanılarak sahte bağlantı noktaları 200Ω 'a dönüştürüldü. Bu iletim hatları, her biri 100Ω ile eşleşecek ve 100Ω sonlandırmaları gerektirecek şekilde ikiyeşerli olarak birleştirildi. Bu bağlantılar, birbirlerine sonlandırma görevi göreceği şekilde yapıldı. Sahte bağlantı noktalarına yapılan bu değişiklik, yan duvar yansımalarını azaltmak için gerekli 50Ω konektörlerin çıkarılmasını mümkün kıldı. Bu sayede tasarımın boyutu ve maliyeti daha da düşürüldü. Geleneksel Rotman Lens tasarımları, sahip olduğu giriş bağlantı noktası sayısına eşit ışın üretebilir. Lensin besleme ağı, iki ekstra ışın oluşturmak için birden fazla girişin birlikte beslenmesine izin veren iletim hatları kullanılarak tasarlandı. Ölçülen ışınlar 9.2 ile 13.7dBi arasında kazançlara sahiptir. Işınlar, 2GHz'lik bir 3dB bant genişliği ile 80° 'lik bir alanı kaplar.

Table of Contents

List of Tables	viii
List of Figures	ix
List of Abbreviations	xii
List of Symbols	xiii
1 INTRODUCTION	1
1.1 Beamforming Networks	1
1.1.1 Digital Beamformers	2
1.1.2 Network Beamformers.....	3
1.1.3 Lenses	3
1.2 Rotman Lens	4
1.2.1 Applications of the Rotman Lens	5
1.3 Objective.....	6
1.4 Thesis Outline	7
2 DESIGN PROCEDURE OF THE ROTMAN LENS	8
2.1 Different Approaches	8
2.1.1 Rotman’s Design	8
2.1.2 Shelton’s Design.....	9

2.1.3	Katagi's Design	10
2.1.4	Gagnon's Design	10
2.1.5	Hansen's Design	11
2.2	Derivations of the Design Equations	11
2.2.1	Waveguide Rotman Lens	11
2.2.2	Microstrip Rotman Lens	17
2.3	Effects of the Design Parameters	21
2.3.1	Focal Ratio	21
2.3.2	Off-Center Focal Angle	21
2.3.3	Maximum Scan Angle	22
3	SIMULATIONS OF THE ROTMAN LENS AND THE AN-	
	TENNA ARRAY	23
3.1	Chosen Design Parameters.....	23
3.1.1	Substrate Selection	24
3.1.2	Choosing the Design Parameters	25
3.2	Simulation Results of the Rotman Lens	27
3.2.1	Return Loss	28
3.2.2	Isolation	29
3.2.3	Phase Adjustments	29
3.3	Simulation Results of the Antenna Array.....	30
3.4	Rotman Lens and Antenna Array Connections	31
3.5	Design of the Slot Coupling.....	33
3.6	Design of the Dummy Ports	36
3.7	Implemented Design	38
3.7.1	Simulation Results of the Implemented Design	38

4	MEASUREMENT RESULTS	43
4.1	Production of the Board	43
4.2	S-Parameter Measurements	44
4.2.1	Glue to Hold the Boards Together	44
4.2.2	Screws to Hold the Boards Together	46
4.2.3	Epoxy to Hold the Boards Together	47
4.3	Far Field Measurements	48
4.3.1	Glue to Hold the Boards Together	49
4.3.2	Screws to Hold the Boards Together	50
4.3.3	Epoxy to Hold the Boards Together	53
5	CONCLUSION	56
	BIBLIOGRAPHY.....	58

List of Tables

Table 2.1	Descriptions of the Design Parameters of the Waveguide Rotman Lens	12
Table 3.1	Design Parameters	24
Table 3.2	Material Properties.....	25
Table 3.3	Selected Design Parameters	26
Table 3.4	3dB Beamwidth at 28GHz	41
Table 3.5	First Sidelobe Levels at 28GHz	42
Table 4.1	3dB Beamwidth	54
Table 4.2	First Sidelobe Level	55

List of Figures

Figure 1.1	Schematic of a beamforming network	2
Figure 1.2	Digital BFN Topology	2
Figure 1.3	Butler Matrix Schematic	3
Figure 1.4	Rotman Lens BFN	4
Figure 1.5	Rotman Lenses used by Raytheon: (a)AN/SLQ-32(V) (b)AN/ALQ-184	5
Figure 1.6	Stacked Rotman Lens	6
Figure 1.7	(a)The Rotman Lens used for imaging; (b)Example Image	6
Figure 2.1	Rotman's Lens Design	9
Figure 2.2	Shelton's Symmetrical Lens Design	9
Figure 2.3	Katagi's Rotman Lens Model	10
Figure 2.4	Waveguide Rotman Lens Parameters	11
Figure 2.5	Beam Contour Parameters	15
Figure 2.6	Microstrip Rotman Lens Parameters	17
Figure 2.7	Effect of "g" on the Lens Contours	21
Figure 2.8	Beam and Inner Lens Contours with Varying α	22
Figure 2.9	Beam and Inner Lens Contours with Varying Maximum Scan Angle	22
Figure 3.1	Lens Geometry	27
Figure 3.2	Signals	27

Figure 3.3	S11 of the Beam Ports	28
Figure 3.4	S11 of the Array Ports	28
Figure 3.5	Isolation Values Between the Beam Ports.....	29
Figure 3.6	Isolation Values Between the Array Ports.....	30
Figure 3.7	View of the 1x10 Antenna Array	31
Figure 3.8	S11 of the 1x10 Antenna Array	31
Figure 3.9	3D View of the Beam Generated at 28GHz	32
Figure 3.10	View of the Rotman Lens with the Transmission Lines Added	33
Figure 3.11	Top View of the Slots	34
Figure 3.12	Side View of the Layers	34
Figure 3.13	Return Loss of the Slot Coupling	35
Figure 3.14	Insertion Loss of the Slot Coupling	35
Figure 3.15	Reflections From the Sidewall	36
Figure 3.16	Conventional Dummy Ports with Connectors Attached.....	37
Figure 3.17	The Dummy Ports Connected Together.....	37
Figure 3.18	Reflection Coefficients of the Dummy Ports.....	38
Figure 3.19	Complete Design	39
Figure 3.20	Slots Opened in the Ground Layer	39
Figure 3.21	Return Loss of the Final Design	40
Figure 3.22	Isolation Values of the Final Design.....	40
Figure 3.23	All Generated Beams.....	41
Figure 3.24	3D Views of the Generated Beams	42
Figure 4.1	Fabricated Array and Rotman Lens.....	44
Figure 4.2	Reflection Coefficients of Board with Glue vs Simulation	45
Figure 4.3	Measured Isolation Values of Board with Glue.....	45
Figure 4.4	Reflection Coefficients of Board with Screws vs Simulation....	46

Figure 4.5	Reflection Coefficients of Board with Epoxy vs Simulation	47
Figure 4.6	The Measurement Setup	48
Figure 4.7	Devices Used for Far Field Measurements	48
Figure 4.8	Normalized Beams at 28GHz	49
Figure 4.9	Maximum Realized Gain vs Frequency	50
Figure 4.10	Normalized Beams at 28GHz	51
Figure 4.11	Normalized Beams at 35GHz	51
Figure 4.12	Measurement Comparison to Simulation with 0.1mm Air Gap(28GHz)	52
Figure 4.13	Measurement Comparison to Simulation with 0.1mm Air Gap(35GHz)	52
Figure 4.14	Normalized Beams at 31GHz	53
Figure 4.15	Maximum Realized Gain vs Frequency	54

List of Abbreviations

A/D analog to digital. 2

BFN beamforming network. ix, 1–5

D/A digital to analog. 2

DUT device under test. 48–51, 53

List of Symbols

(X_b, Y_b)	Coordinates of the Array Elements
α	Off-center Focal Angle
$\Delta\Phi$	Phase Difference Between Adjacent Array Elements
ϵ	Substrate Permittivity
η	Normalized Coordinates of the Array Elements
λ	Wavelength
Σ_1	Inner Receiver Contour
Σ_2	Outer Lens Contour
θ	Scan Angle
a_0	$\cos \alpha$
b_0	$\sin \alpha$
d	Distance Between Adjacent Array Elements
F_1, F_2	Off-axis Focal Points
g	Normalized On-axis Focal Length
w	Normalized Difference of the Length of Transmission Lines Between Array Elements and Inner Receiver Contour
x, y	Normalized Coordinates of the Receiver Port Phase Centers
(X, Y)	Coordinates of the receiver port phase centers
a, b	Radii of the Ellipse
e	Eccentricity of Ellipse

F	On-axis Focal Length
G	On-axis Focal Length
G_0	On-axis Focal Point
N	Coordinates of the Array Elements
W	Length of the transmission line between receivers and array elements
W_0	Length of the transmission line between receivers and array elements through the origin

Chapter 1

INTRODUCTION

Phased arrays, used widely in communication systems, are systems capable of outputting multiple beams. With the developments in the communication systems over the years, they are getting more and more important. These systems combine an antenna array and a circuit that can have multiple outputs with phase differences to generate multiple beams.

In a phased array, these phase differences are generated by a beamforming network. A beamforming network is a circuit that has multiple outputs and inputs. Each input determines the phase difference that the network will cause, and when these outputs with phase differences are fed into an antenna array, different beams can be generated.

1.1 Beamforming Networks

A beamforming network is a circuit that controls not only the amplitudes, but also the phase differences between its outputs. Generally, a beamforming network has multiple inputs and outputs. An example diagram of a typical beamformer can be seen in Figure 1.1. The number and locations of the input and output ports can be adjusted to suit the design. The output ports are then connected to the inputs of the antenna array, and when the correct inputs feeds are given, a beam will be generated.

For this thesis, different beamforming networks will be categorized as presented in [1]. Hansen divides beamforming networks into three categories; digital beamformers, network beamformers and lenses.

In the following chapters “beamforming network” will be abbreviated as BFN.

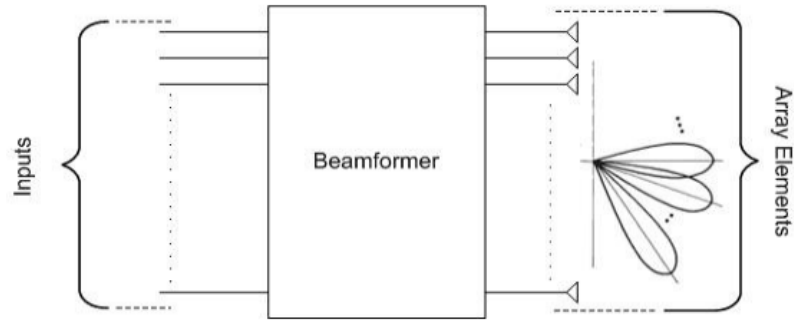


Figure 1.1 Schematic of a beamforming network

1.1.1 Digital Beamformers

Digital BFN's utilize a processor to control the phase differences that they can generate. A digital BFN has additional components compared to other types of BFN's. Because they use digital signals to control the phase, they require converters to change the input signal to digital. This is done by the use of analog to digital (A/D) converters. After the signal is converted to digital, the BFN uses the control input coming from the processor to adjust the phase of the signal. Since the phase adjusting process is controlled by a processor, one can also manipulate the amplitude of the signal. After the phase is adjusted, the digital signal is once again converted to analog, by using a digital to analog (D/A) converter. A typical digital BFN can be seen in Figure 1.2.

The limitations of this type of BFN comes from the processor and the two converters. With the increase in frequency resulting from the usage of new communication protocols (such as 5G), the processors also need to get faster. This is because handling RF data requires faster processors. The converters also need to be able to adapt to the needs of communication systems. The usage of A/D converters can be limited because of their dynamic range. An A/D converter needs high dynamic range to be used in communication systems [1].

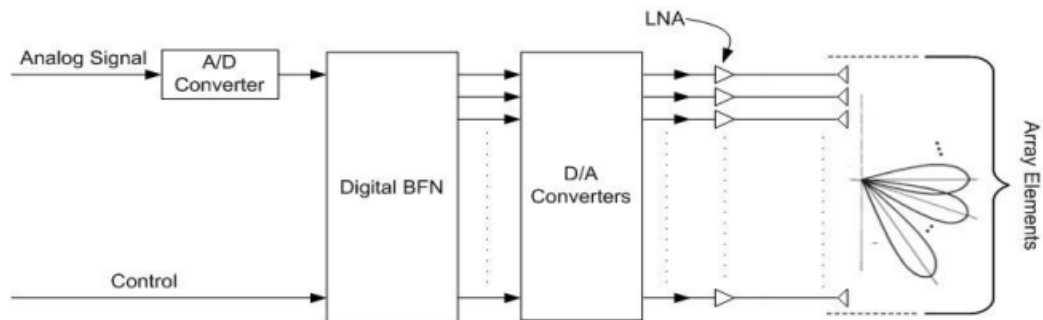


Figure 1.2 Digital BFN Topology

1.1.2 Network Beamformers

Network BFN's are analog circuits that generally use phase shifters and hybrid junctions. An example of a network BFN can be seen in Figure 1.3, which is a Butler Matrix. The Butler Matrix is one of the most commonly used type of network BFN. A Butler Matrix connects 2^n inputs to the same number of outputs. It has its advantages in being easy to fabricate, using transmission lines, but there are conductor crossovers that are required. In more complicated designs these crossovers might require multi-layer layout which can complicate the fabrication process. One of the disadvantages of the network BFN is that it is frequency dependent, which produces a limited bandwidth. Hence, its performance becomes limited depending on its components. As frequency changes, the beamwidths and beam angles it produces also shifts. If the system requires higher frequency ranges, using a network BFN can be disadvantageous [1].

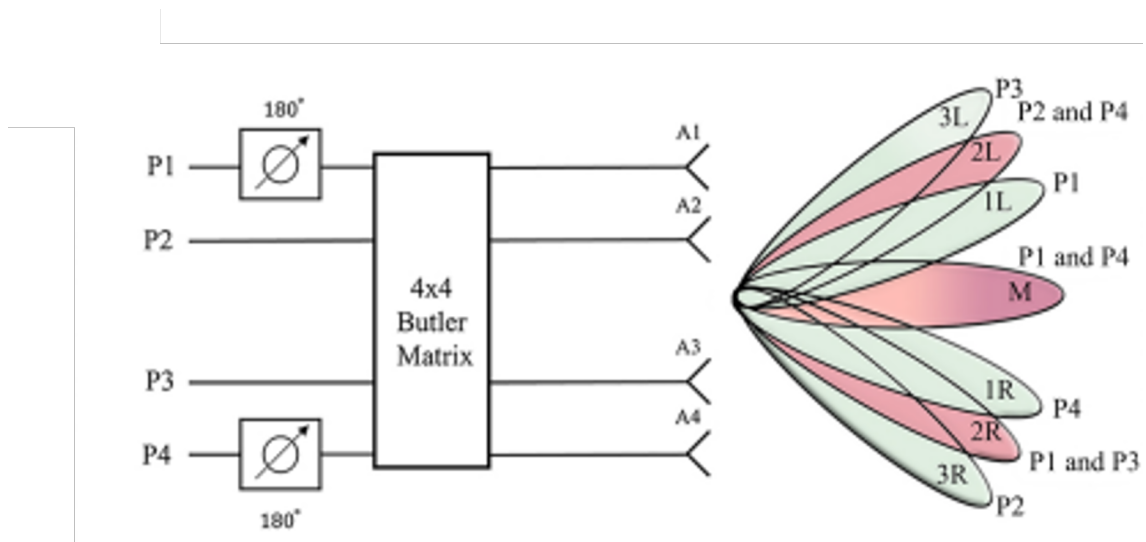


Figure 1.3 Butler Matrix Schematic

1.1.3 Lenses

The lens BFN's utilize the path delay between the input and output ports to achieve the desired amplitude and phase shift. A typical lens BFN structure can be seen in Figure 1.4. It consists of input ports, beam ports, lens cavity, and receiving ports. The beam ports radiate the signal within the lens cavity, where the path delay is applied upon the signal. The signal then goes through the receiving ports which are then fed into the antenna array. The locations of the beam and receiving ports are what determines the path delay of this type of BFN. Their placements, along with the length of the transmission lines, can be changed to achieve the wanted phase shift and amplitude of the radiated beams.

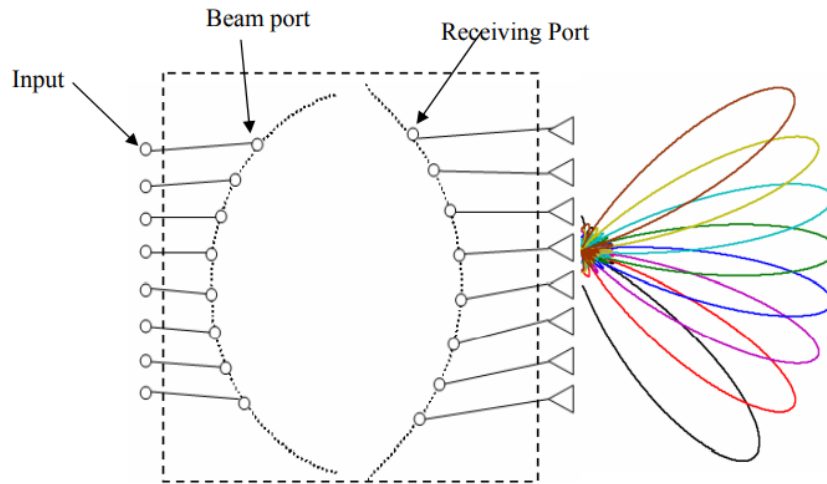


Figure 1.4 Rotman Lens BFN

In Figure 1.4, eight different beams can be seen as being possibly radiated from the antenna array. Each one of these eight beams correspond to one of the input ports of the BFN. The number of beam ports of a lens BFN determines the beams that it can generate.

Because the lens BFN uses path delay mechanism, which is independent from frequency, they can be used in wideband applications. They can also be realized using waveguides or microstrip lines. If handling higher power levels is required, waveguides can be used. If a lower profile is desired, microstrip lines can be used. The lens BFN can be designed differently according to the requirements.

Generalized equations for the lens BFN was given by Gent [2]. Using these equations, the Rotman Lens was developed by Rotman and Turner [3].

1.2 Rotman Lens

The Rotman Lens was developed by Rotman and Turner in 1963 [3]. Their design improved upon the equations that were given by Gent [2] and investigated by Ruze [4]. Their design had three focal points and due to this reason, lenses that are tri-focal are labelled as Rotman Lenses. The design that Rotman published was a lens that used waveguides. After using printed circuit technologies was suggested by Archer to have lower profile lenses [5], studies into using microstrip lines for the Rotman Lens increased.

The work done by Rotman and Turner continues to be the benchmark for research about the Rotman Lens. However, several different design approaches have been

suggested over the years. Some of these designs will be explained further in Chapter 2, before going over the design procedures of the Rotman Lens.

1.2.1 Applications of the Rotman Lens

Lens BFN's can be used for radars, both airborne and marine. Raytheon Electronic Warfare used Rotman Lenses in marine radars, such as AN/SLQ-32(V), which was used in over 450 U.S. Navy ships [6]. An example for the airborne applications is the AN/ALQ-184, an electronic warfare pod, once again developed by Raytheon Electronic Warfare.



Figure 1.5 Rotman Lenses used by Raytheon: (a)AN/SLQ-32(V) (b)AN/ALQ-184

Rotman Lenses are designed for two-dimensional scans, but they can also be used in applications that require three-dimensional scanning capabilities. To do this, several Rotman Lenses need to be stacked together. A Rotman Lens by itself generates a fan shaped beam. However, by feeding the inputs of a Rotman Lens through other Rotman Lenses, it is possible to generate pencil shaped beams. An example of this can be seen in Figure 1.6. The generation of pencil beams opens new application areas for the Rotman Lens, such as satellite communications [7].

Lens BFN's can also be used in photonic imaging systems. This was first proposed by Steyskal [8]. They are passive, have wide angle scanning capabilities and are true time delay devices, which means they are not dependent on frequency. An example of this can be seen in [9]. In their paper, they built a detector that utilizes a Rotman Lens for its phase processor. The designed Rotman Lens and one of the example pictures taken using the device can be seen in Figure 1.7 [9].

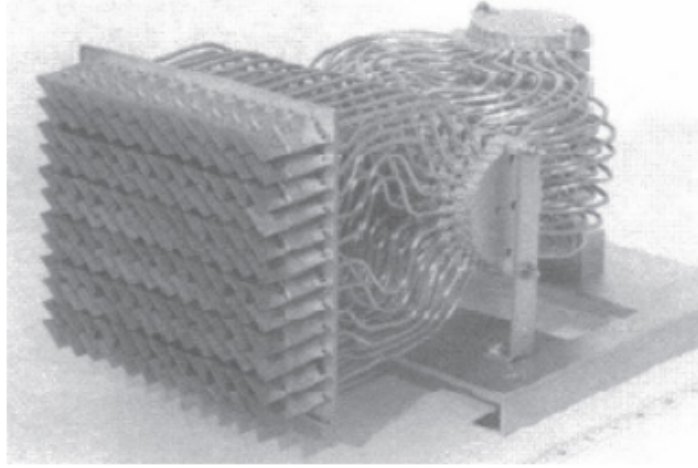


Figure 1.6 Stacked Rotman Lens

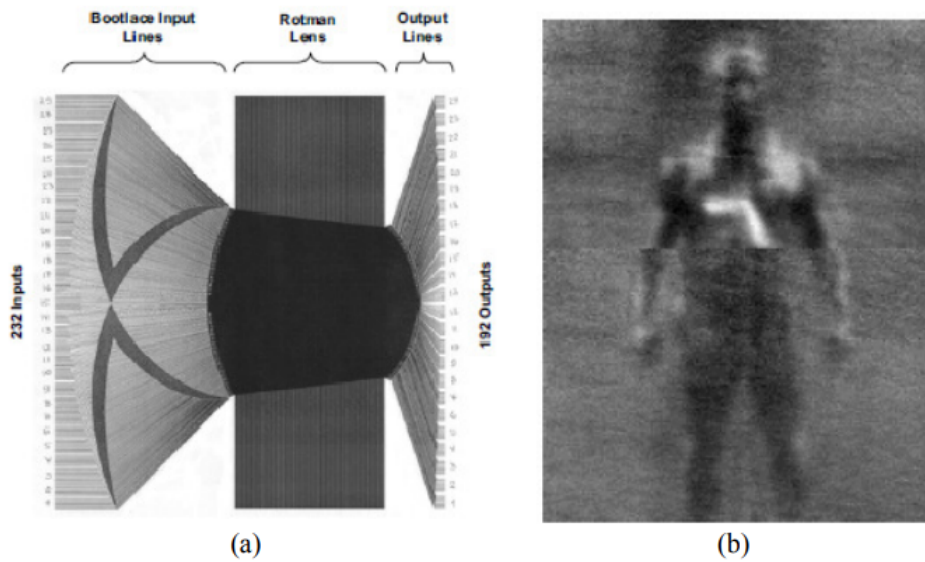


Figure 1.7 (a)The Rotman Lens used for imaging; (b)Example Image

1.3 Objective

In this thesis, different approaches to the Rotman Lens design are presented, and in accordance with the research a Rotman Lens was designed and fabricated to be measured within the facilities at Sabanci University. So, the goal of this study was to design a microstrip Rotman Lens and verify the results by doing the relevant measurements.

1.4 Thesis Outline

This thesis will consist of five chapters:

In the first chapter, general information about beamforming networks is given. Some of the applications of the Rotman Lens are also presented.

In the second chapter, different Rotman Lens designs will be presented, the equations of the design process will be derived, the design parameters will be explained and the effects of these parameters on the Rotman Lens geometry will be shown.

In the third chapter, the chosen parameters for the Rotman Lens and the design of the transmission lines will be shown, the coupling of the Rotman Lens and the antenna array will be presented, and the adjustments made on the dummy ports will be demonstrated. The simulation results of the designed Rotman Lens and antenna array will also be given.

In the fourth chapter, the measurement results, and their comparisons to the simulations, of different board structures will be given.

In the fifth chapter, conclusions about the project will be presented.

Chapter 2

DESIGN PROCEDURE OF THE ROTMAN LENS

In this chapter, the design procedures of the Rotman Lens are presented. Different design approaches will be shown [10], afterwards the equations that was presented in [3] will be derived. Then, the parameters of these equations will be investigated and the effect they have on the lens geometry and performance will be shown.

2.1 Different Approaches

2.1.1 Rotman's Design

In Rotman's approach to the design, the general lens equations presented by Gent [2] is used. The parameters of the design can be seen in Figure 2.1. The feeds of the lens are located on the beam contour, denoted as circular focal arc in Figure 2.1. The inner lens contour, also called the array contour, contains the receiving elements of the lens, and the array elements are located on the outer lens contour. There are three focal points on the focal arc, one on-axis focal point (G) and two symmetrical off-axis focal points (F_1 and F_2).

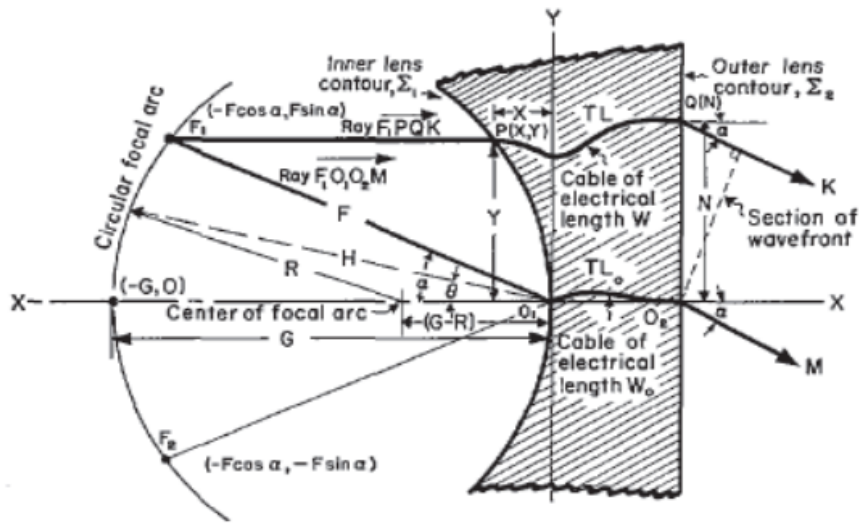


Figure 2.1 Rotman's Lens Design

2.1.2 Shelton's Design

The lens configuration seen in Figure 2.3 was developed by Shelton [11] as a modification to the Rotman Lens. The array and beam contours are symmetrical. This design is better for applications that require similar number of array and beam ports.

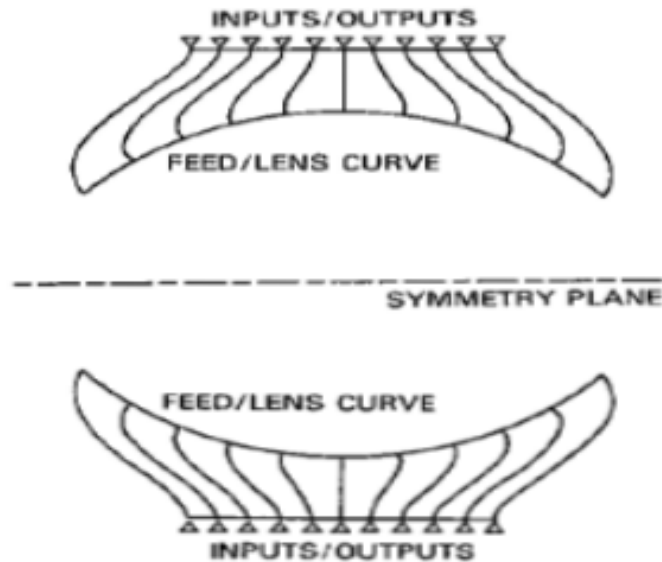


Figure 2.2 Shelton's Symmetrical Lens Design

2.1.3 Katagi's Design

In 1984, a new design approach was suggested by Katagi [12]. In this approach, a new variable was introduced to the design of the Rotman Lens. As seen in Figure 2.3, just like in Rotman's model, a subtended angle (α) is defined as corresponding to one of the off-axis focal points. However, unlike Rotman's model, the scan angle (β), which is the angle of the output beam when F1 is excited, is not assumed to be the same as the subtended angle. This way, the ratio of the subtended angle and the scan angle defines a new parameter for the design of the Rotman Lens. The introduction of this new parameter introduces another degree of freedom to the design process of the Rotman Lens. Katagi also suggested that the shape of the beam contour does not have to be circular and showed that changing the circular shape of the beam contour can lower the phase errors compared to Rotman's original design [12].

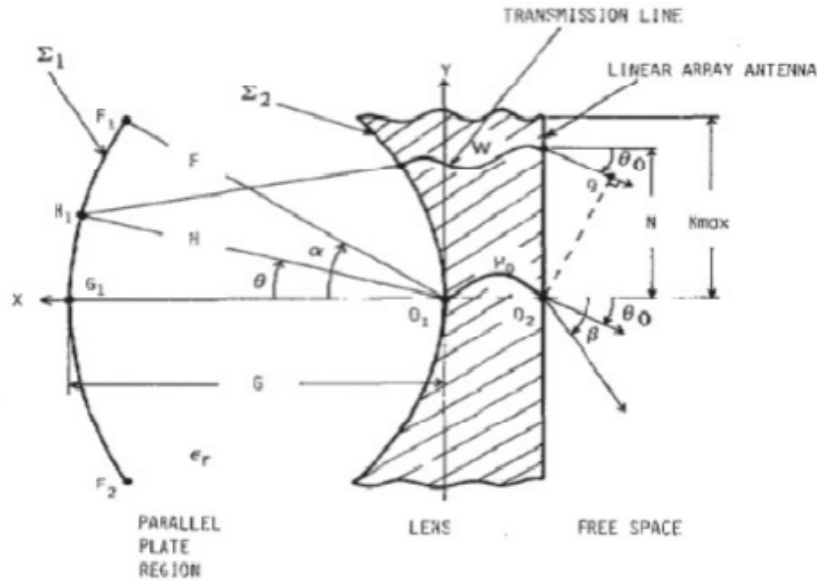


Figure 2.3 Katagi's Rotman Lens Model

2.1.4 Gagnon's Design

Gagnon's [13] approach was to introduce refocusing procedure according to Snell's law for the Rotman Lens's that were filled with a dielectric material. Applying Snell's law yields a ratio of $\sqrt{\epsilon}$ between the sine values of the subtended angle and the scan angle. This approach made it possible to improve the coupling of the outermost beam ports, especially for printed lenses used with smaller arrays, by providing better beam and array port positions.

2.1.5 Hansen's Design

Hansen [14] used six parameters for the design of the Rotman Lens. These parameters were focal angle, focal ratio, beam angle (subtended angle) to ray angle (scan angle) ratio, maximum subtended angle, focal length, and array element spacing. Another parameter called ellipticity was also introduced, which assumed that the lens contours were elliptical instead of circular. The two parameters ellipticity and beam angle to ray angle ratio were additions to the parameters used by Rotman in the original design. The effects of these design parameters on the shape of the Rotman Lens, as well as their effects on the amplitude errors were explained in detail.

2.2 Derivations of the Design Equations

In this section, the equations that the Rotman Lens design is based on will be derived. First, Rotman's [3] approach will be used to derive the equations of a waveguide Rotman Lens. Afterwards, the equations for the microstrip based Rotman Lens will be derived. The equations of the microstrip Rotman Lens will be based on Rotman's work, with the addition of the dielectric properties of the material used.

2.2.1 Waveguide Rotman Lens

Rotman's [3] design will be used to derive the equations of the waveguide Rotman Lens. The design parameters of the Rotman Lens can be seen below in Figure 2.4. These parameters will be used to derive the equations.

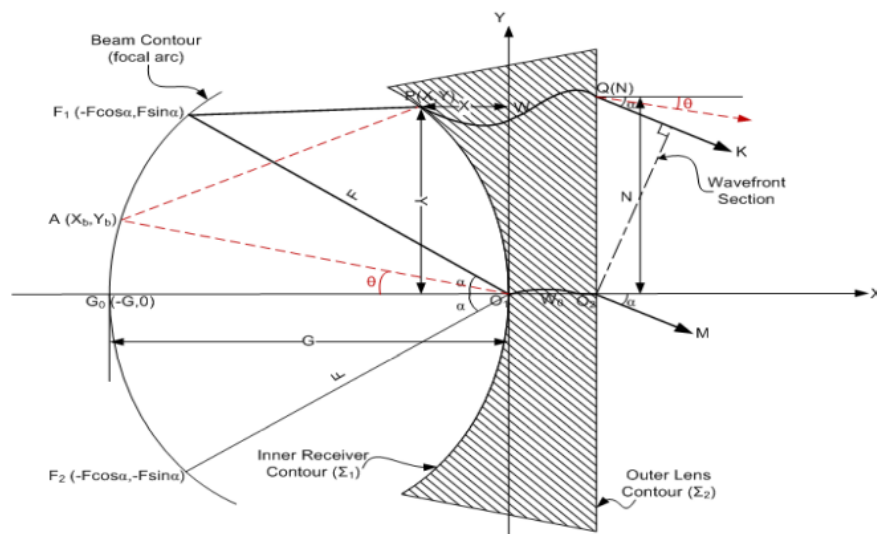


Figure 2.4 Waveguide Rotman Lens Parameters

The parameters shown in Figure 2.4 can be seen with their descriptions in Table 2.1. From these parameters, F , G , N , and α are to be chosen by the designer, and X , Y , W , X_b and Y_b are to be calculated using the equations to draw the geometry of the lens.

Table 2.1 Descriptions of the Design Parameters of the Waveguide Rotman Lens

F	Off-Axis Focal Length
G	On-Axis Focal Length
α	Off-Center Focal Angle
θ	Scan Angle
F_1, F_2	Off-Axis Focal Points
G_0	On-Axis Focal Point
W_0	Length of the transmission line between receivers and array elements through the origin
W	Length of the transmission line between receivers and array elements
X, Y	Coordinates of the receiver port phase centers
N	Coordinates of the Array Elements
X_b, Y_b	Coordinates of the beam port phase centers

The phase centers of the receivers are located on the inner receiver contour (Σ_1), and the outer lens contour (Σ_2), which is chosen as a straight line, is the positions of the array elements.

The coordinates on Σ_1 are defined by (X,Y) pairs, where $P(X,Y)$ is an arbitrary point on the contour. The coordinates on Σ_2 are defined by a single variable N , where $Q(N)$ is an arbitrary point on the contour. N is determined by the placements of the array elements, so it should be defined before starting the calculations. The two contours, specifically point $P(X,Y)$ and point $Q(N)$, will be connected together via transmission lines that have electrical lengths of W . Because of this, X , Y and W should be calculated in terms of other design parameters.

In the design of the contour Σ_1 three focal points are used. One on-axis focal point (G_0) and two symmetrical off-axis focal points (F_1 and F_2). To derive the equations, optical path-length equality and geometric relations are written.

From the optical path-length equality between a ray travelling the path $(\overrightarrow{F_1PQK})$ and the ray going through the origin $(\overrightarrow{F_1O_1O_2M})$ we get:

$$(\overrightarrow{F_1P}) + W + N \sin \alpha = F + W_0, \quad (2.1)$$

$$(\overrightarrow{F_2P}) + W - N \sin \alpha = F + W_0, \quad (2.2)$$

$$(\overrightarrow{G_0P}) + W = G + W_0, \quad (2.3)$$

From the geometrical relations we get:

$$(\overrightarrow{F_1P})^2 = F^2 + X^2 + Y^2 + 2FX \cos \alpha - 2FY \sin \alpha, \quad (2.4)$$

$$(\overrightarrow{F_2P})^2 = F^2 + X^2 + Y^2 + 2FX \cos \alpha + 2FY \sin \alpha, \quad (2.5)$$

$$(\overrightarrow{G_0P})^2 = (G + X)^2 + Y^2, \quad (2.6)$$

To simplify the equations, the parameters are normalized with respect to the focal length F. The normalized parameters are as follows:

$$\eta = \frac{N}{F}, \quad x = \frac{X}{F}, \quad y = \frac{Y}{F}, \quad w = \frac{W - W_0}{F}, \quad g = \frac{G}{F}$$

To further simplify the equations, new intermediate parameters are also introduced:
 $a_0 = \cos \alpha, b_0 = \sin \alpha$

Normalizing the equations 2.1 to 2.6 with respect to F we get:

$$\frac{(\overrightarrow{F_1P})}{F} = 1 - w - \eta b_0, \quad (2.7)$$

$$\frac{(\overrightarrow{F_2P})}{F} = 1 - w + \eta b_0, \quad (2.8)$$

$$\frac{(\overrightarrow{G_0P})}{F} = g - w, \quad (2.9)$$

$$\frac{(\overrightarrow{F_1 P})^2}{F^2} = 1 + x^2 + y^2 + 2a_0x - 2b_0y, \quad (2.10)$$

$$\frac{(\overrightarrow{F_2 P})^2}{F^2} = 1 + x^2 + y^2 + 2a_0x + 2b_0y, \quad (2.11)$$

$$\frac{(\overrightarrow{G_0 P})^2}{F^2} = (g+x)^2 + y^2, \quad (2.12)$$

Taking the square of the equations 2.7 to 2.9 and equating them to equations 2.10 to 2.12 gives us:

$$(1 - w - \eta b_0)^2 = 1 + x^2 + y^2 + 2a_0x - 2b_0y, \quad (2.13)$$

$$(1 - w + \eta b_0)^2 = 1 + x^2 + y^2 + 2a_0x + 2b_0y, \quad (2.14)$$

$$(g - w)^2 = (g + x)^2 + y^2, \quad (2.15)$$

Equations 2.13 to 2.15 can be written explicitly to write the variables in terms of each other:

$$w^2 - 2w + 2b_0\eta w + b_0^2\eta^2 - 2b_0\eta = x^2 + y^2 + 2a_0x - 2b_0y, \quad (2.16)$$

$$w^2 + 2w - 2b_0\eta w + b_0^2\eta^2 + 2b_0\eta = x^2 + y^2 + 2a_0x + 2b_0y, \quad (2.17)$$

$$w^2 - 2gw = x^2 + y^2 + 2gx, \quad (2.18)$$

From 2.16 and 2.17 we get:

$$y = \eta(1 - w), \quad (2.19)$$

$$w^2 - 2w + b_0^2\eta^2 = x^2 + y^2 + 2a_0x, \quad (2.20)$$

Substitute 2.19 in 2.18:

$$x = -\frac{(g-1)}{(g-a_0)}w - \frac{(b_0^2\eta^2)}{2(g-a_0)}, \quad (2.21)$$

After manipulating 2.18 and 2.20, we can get the relation between w and :

$$aw^2 + bw + c = 0, \quad (2.22)$$

where;

$$a = [1 - \eta^2 - (\frac{(g-1)}{(g-a_0)})^2]$$

$$b = [2g(\frac{(g-1)}{(g-a_0)}) - (\frac{(g-1)}{(g-a_0)})b_0^2\eta^2 + 2\eta^2] - 2g$$

$$c = [(\frac{gb_0^2\eta^2}{(g-a_0)}) - (\frac{(b_0^4\eta^4)}{4(g-a_0)^2}) - \eta^2]$$

Using equation 2.22, w can be written with respect to η when α and g are fixed. To determine the values of x and y , w and η can be substituted into equations 2.19 and 2.21.

With the equations for the parameters for the inner contour derived, the equations for the beam contour can now be derived. The beam contour is assumed to have an elliptical shape that passes through all three focal points. To derive the equations for the beam contour, the elliptical shape it has needs to be defined, with new parameters that determine its shape. The new parameters can be seen in Figure 2.5.

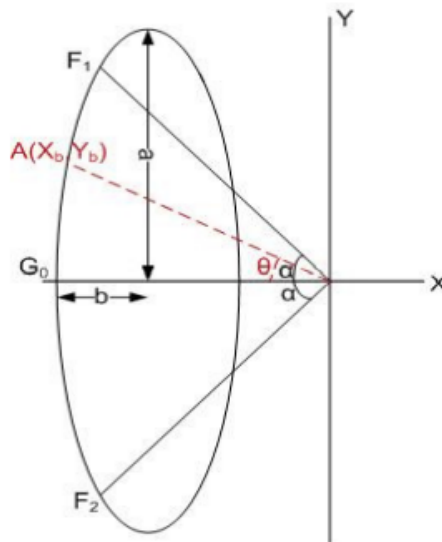


Figure 2.5 Beam Contour Parameters

To be able to derive the equations for the beam contour, the equation for the ellipse needs to be written. The equation that defines the ellipse seen in Figure 2.5 is as follows:

$$\frac{(x + g - b)^2}{b^2} + \frac{y^2}{b^2} = 1, \quad (2.23)$$

To define the ellipse, its eccentricity needs to be defined:

$$e = \sqrt{\frac{a^2 - b^2}{a^2}}, \quad (2.24)$$

Using the eccentricity equation, b can be written in terms of a and e:

$$b^2 = a^2(1 - e^2), \quad (2.25)$$

By substituting 2.25 into 2.23 we get:

$$(x + g - a\sqrt{1 - e^2})^2 + y^2(1 - e^2) = a^2(1 - e^2), \quad (2.26)$$

All of the focal points are on the beam contour, so a can be calculated by using the coordinates of the off-axis foci:

$$a = \frac{(e \sin \alpha)^2 + 2g \cos \alpha - g^2 - 1}{\sqrt{1 - e^2}(2 \cos \alpha - 2g)}, \quad (2.27)$$

For a given e and θ , the coordinates (x_b, y_b) can be found by substituting y_b with $y_b = -x_b \tan \theta$. Then, using the equation 2.26, x_b and y_b can be computed from equations 2.28 and 2.29, where a is calculated using 2.27.

$$[1 + (1 - e^2) \tan^2 \theta] x_b^2 + (2g - 2a\sqrt{1 - e^2}) x_b + g^2 - 2ag\sqrt{1 - e^2} = 0, \quad (2.28)$$

$$y_b = -x_b \tan \theta, \quad (2.29)$$

$$\sqrt{\epsilon_r}(\overrightarrow{F_1P}) + \sqrt{\epsilon_{re}}W + N \sin \alpha = \sqrt{\epsilon_r}F + \sqrt{\epsilon_{re}}W_0, \quad (2.30)$$

$$\sqrt{\epsilon_r}(\overrightarrow{F_1P}) + \sqrt{\epsilon_{re}}W - N \sin \alpha = \sqrt{\epsilon_r}F + \sqrt{\epsilon_{re}}W_0, \quad (2.31)$$

$$\sqrt{\epsilon_r}(\overrightarrow{G_0P}) + \sqrt{\epsilon_{re}}W = \sqrt{\epsilon_r}G + \sqrt{\epsilon_{re}}W_0, \quad (2.32)$$

From the geometrical relations we get:

$$(\overrightarrow{F_1P})^2 = F^2 + X^2 + Y^2 + 2FX \cos \alpha - 2FY \sin \alpha, \quad (2.33)$$

$$(\overrightarrow{F_2P})^2 = F^2 + X^2 + Y^2 + 2FX \cos \alpha + 2FY \sin \alpha, \quad (2.34)$$

$$(\overrightarrow{G_0P})^2 = (G + X)^2 + Y^2, \quad (2.35)$$

To simplify the equations, the parameters are normalized with respect to the focal length F. The normalized parameters are as follows:

$$\eta = \frac{N}{F}, \quad x = \frac{X}{F}, \quad y = \frac{Y}{F}, \quad w = \frac{W - W_0}{F}, \quad g = \frac{G}{F}$$

To further simplify the equations, new intermediate parameters are also introduced:
 $a_0 = \cos \alpha, b_0 = \sin \alpha$

Normalizing the equations 2.30 to 2.35 with respect to F we get:

$$\sqrt{\epsilon_r} \frac{(\overrightarrow{F_1P})}{F} = \sqrt{\epsilon_r} - \sqrt{\epsilon_{re}}w - \eta b_0, \quad (2.36)$$

$$\sqrt{\epsilon_r} \frac{(\overrightarrow{F_2P})}{F} = \sqrt{\epsilon_r} - \sqrt{\epsilon_{re}}w + \eta b_0, \quad (2.37)$$

$$\sqrt{\epsilon_r} \frac{(\overrightarrow{G_0P})}{F} = \sqrt{\epsilon_r}g - \sqrt{\epsilon_{re}}w, \quad (2.38)$$

$$\frac{(\overrightarrow{F_1 P})^2}{F^2} = 1 + x^2 + y^2 + 2a_0x - 2b_0y, \quad (2.39)$$

$$\frac{(\overrightarrow{F_2 P})^2}{F^2} = 1 + x^2 + y^2 + 2a_0x + 2b_0y, \quad (2.40)$$

$$\frac{(\overrightarrow{G_0 P})^2}{F^2} = (g + x)^2 + y^2, \quad (2.41)$$

Taking the square of the equations 2.36 to 2.38 and equating them to equations 2.39 to 2.41 gives us:

$$\left(1 - \frac{\sqrt{\epsilon_{re}}}{\sqrt{\epsilon_r}}w - \frac{\eta b_0}{\sqrt{\epsilon_r}}\right)^2 = 1 + x^2 + y^2 + 2a_0x - 2b_0y, \quad (2.42)$$

$$\left(1 - \frac{\sqrt{\epsilon_{re}}}{\sqrt{\epsilon_r}}w + \frac{\eta b_0}{\sqrt{\epsilon_r}}\right)^2 = 1 + x^2 + y^2 + 2a_0x + 2b_0y, \quad (2.43)$$

$$\left(g - \frac{\sqrt{\epsilon_{re}}}{\sqrt{\epsilon_r}}w\right)^2 = (g + x)^2 + y^2, \quad (2.44)$$

Equations 2.13 to 2.15 can be written explicitly to write the variables in terms of each other:

$$\frac{\sqrt{\epsilon_{re}}}{\sqrt{\epsilon_r}}w^2 - 2\frac{\sqrt{\epsilon_{re}}}{\sqrt{\epsilon_r}}w + 2\frac{\sqrt{\epsilon_{re}}}{\sqrt{\epsilon_r}}b_0\eta w + \frac{b_0^2\eta^2}{\epsilon_r} - \frac{b_0\eta}{\sqrt{\epsilon_r}} = x^2 + y^2 + 2a_0x - 2b_0y, \quad (2.45)$$

$$\frac{\sqrt{\epsilon_{re}}}{\sqrt{\epsilon_r}}w^2 + 2\frac{\sqrt{\epsilon_{re}}}{\sqrt{\epsilon_r}}w - 2\frac{\sqrt{\epsilon_{re}}}{\sqrt{\epsilon_r}}b_0\eta w + \frac{b_0^2\eta^2}{\epsilon_r} + \frac{b_0\eta}{\sqrt{\epsilon_r}} = x^2 + y^2 + 2a_0x + 2b_0y, \quad (2.46)$$

$$\frac{\epsilon_{re}}{\epsilon_r}w^2 - 2g\frac{\sqrt{\epsilon_{re}}}{\sqrt{\epsilon_r}}w = x^2 + y^2 + 2gx, \quad (2.47)$$

Manipulating 2.45 and 2.46 we get:

$$y = \frac{\eta}{\sqrt{\epsilon_r}} \left(1 - \frac{\sqrt{\epsilon_{re}}}{\sqrt{\epsilon_r}} w\right), \quad (2.48)$$

$$\frac{\epsilon_{re}}{\epsilon_r} w^2 - 2 \frac{\sqrt{\epsilon_{re}}}{\sqrt{\epsilon_r}} w + \frac{b_0^2 \eta^2}{\epsilon_r} = x^2 + y^2 + 2a_0 x, \quad (2.49)$$

By substituting 2.48 in 2.47:

$$x = -\frac{\sqrt{\epsilon_{re}}}{\sqrt{\epsilon_r}} \frac{(g-1)}{(g-a_0)} w - \frac{(b_0^2 \eta^2)}{2(g-a_0)\epsilon_r}, \quad (2.50)$$

After manipulating 2.47 and 2.49, we can get the relation between w and :

$$aw^2 + bw + c = 0, \quad (2.51)$$

where;

$$a = \left[\frac{\epsilon_{re}}{\epsilon_r} \left(1 - \frac{\eta^2}{\epsilon_r} - \left(\frac{g-1}{g-a_0}\right)^2 \right) \right]$$

$$b = \left[\frac{\sqrt{\epsilon_{re}}}{\sqrt{\epsilon_r}} \left(2g \left(\frac{g-1}{g-a_0}\right) - 1\right) - \left(\frac{g-1}{g-a_0}\right) b_0^2 \frac{\eta^2}{\epsilon_r} + 2 \frac{\eta^2}{\epsilon_r} \right]$$

$$c = \left[\left(\frac{g b_0^2 \eta^2}{(g-a_0)\epsilon_r}\right) - \left(\frac{b_0^4 \eta^4}{4\epsilon_r^2 (g-a_0)^2}\right) - \frac{\eta^2}{\epsilon_r} \right]$$

Using equation 2.51, w can be written with respect to η when α and g are fixed. To determine the values of x and y , w and η can be substituted into equations 2.48 and 2.50.

As an alternative to the derivations done for the microstrip Rotman Lens equations, the variables w and η can be replaced with $\frac{\sqrt{\epsilon_{re}}}{\sqrt{\epsilon_r}} w$ and $\frac{1}{\sqrt{\epsilon_r}} \eta$.

2.3 Effects of the Design Parameters

2.3.1 Focal Ratio

The focal ratio is the ratio of the on-axis focal length to the off-axis focal length. The change in focal ratio affects both the beam contour and the inner lens contour. The changes observed on the contours with varying g can be seen in Figure 2.7.

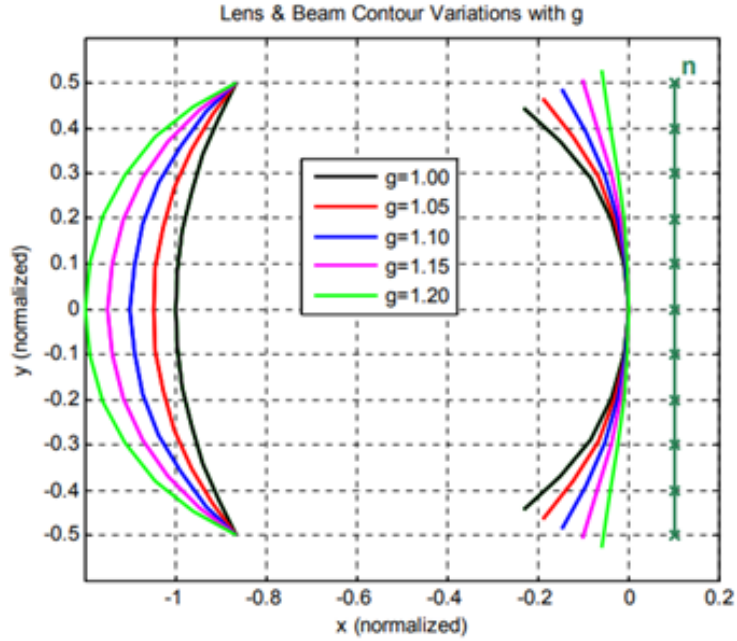


Figure 2.7 Effect of "g" on the Lens Contours

In [4], it is shown that for straight front face lenses with focal ratios greater than 0.8, the refocusing needed to minimize the phase error is equal to $\frac{1}{2}(\alpha^2 - \theta^2)F$, where θ is the angle at which correction is needed. Using this formula, the optimum g value when $\theta = 0^\circ$ is equal to:

$$g = 1 + \frac{\alpha^2}{2}, \quad (2.52)$$

2.3.2 Off-Center Focal Angle

Similar to the focal ratio, the off-center focal angle also affects both of the contours. When the other parameters are fixed, the changes observed on the off-center focal angle changes the curvatures of the contours. As seen in Figure 2.8, the bending of the beam contour increases with decreasing off-center focal angle, and the bending of the inner lens contour decreases together with the off-center focal angle [15] [16].

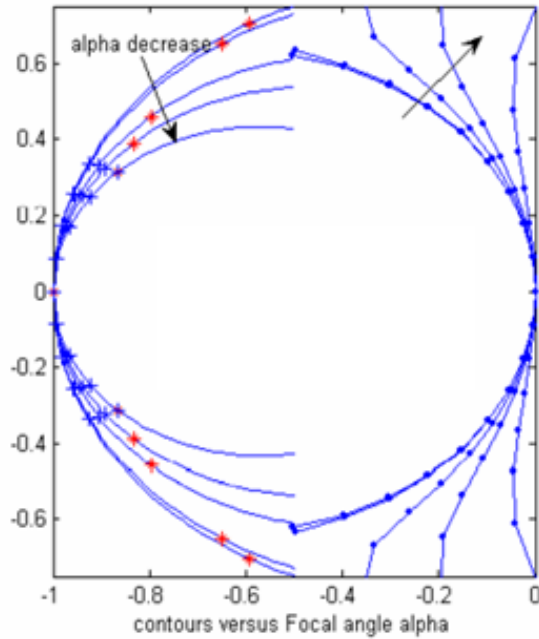


Figure 2.8 Beam and Inner Lens Contours with Varying α

2.3.3 Maximum Scan Angle

As the maximum scan angle increases, so does the path-length delay that a signal needs to go through within the Rotman Lens. While the other parameters are fixed, this increase in path-length delay is compensated by changing the placement of the phase centers of the beam ports.

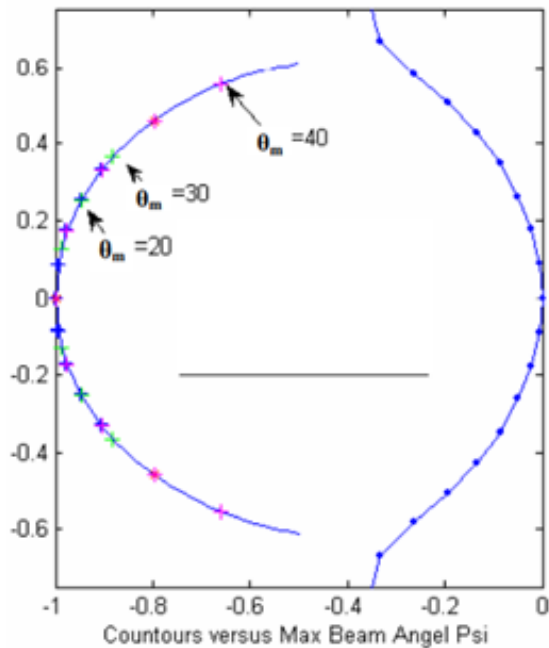


Figure 2.9 Beam and Inner Lens Contours with Varying Maximum Scan Angle

Chapter 3

SIMULATIONS OF THE ROTMAN LENS AND THE ANTENNA ARRAY

In this chapter, the simulation results of the designed Rotman Lens and the antenna array will be presented. Firstly, the chosen design parameters will be explained. Afterwards, the simulation results of different design steps will be shown. These steps include the simulations of the initial S-Parameters of the Rotman Lens, the changes that were observed after the addition of the transmission lines and the beams that were produced after the Rotman Lens and the antenna array were connected together. The design of the slots used to couple the Rotman Lens and the antenna array, and their effect on the beams that were produced will also be shown. Afterwards, the changes made to the conventional Rotman Lens design by doing adjustments to the dummy ports will be explained.

For this thesis, a Rotman Lens is designed using microstrip lines as opposed to waveguides. By using microstrip lines instead of waveguides, the size of the lens was reduced because of the substrate permittivity (ϵ_r). The choice of using microstrip technologies also makes the fabrication process easier.

3.1 Chosen Design Parameters

The first thing to decide when designing a Rotman Lens is the target requirements. In this thesis, the microstrip Rotman Lens was designed to satisfy the requirements seen in Table 3.1.

Table 3.1 Design Parameters

Center Frequency	28GHz
Scan Angle	$\pm 30^\circ$
Number of Beam Ports	5
Number of Array Ports	6

With the target requirements chosen, the next thing to decide is the material that will be used as the substrate. The permittivity of the substrate directly affects the design of the Rotman Lens, because of the equations used in the design process. The change in dielectric permittivity not only affects the locations of the port phase centers, but also the overall size of the design. After the substrate is chosen, other parameters can be determined using the design equations to optimize path-length errors.

Afterwards, transmission lines are designed to make the connections between the Rotman Lens, the antenna array, and the input connectors. The transmission lines are designed to have the same length so that the phase differences between the array ports are not changed. If required, the transmission lines can also be adjusted so that the required phase differences are achieved at the output of the Rotman Lens.

With the transmission lines designed, the antenna array is then connected. In this thesis, the array is coupled to the Rotman Lens by opening slots through the ground layer, creating a design that is three layered and decreasing the overall size of the design. The designed slots will be discussed further in this chapter.

In this thesis, the design process flows as described. However, unlike conventional Rotman Lens designs, the dummy ports at the sides of the Rotman Lens were also modified. The changes made to these ports will be shown in detail further in this chapter.

3.1.1 Substrate Selection

For the selection of the dielectric material, the thickness of the material and the permittivity should be considered. The permittivity of the material is a parameter that can control the size of the Rotman Lens since the path-lengths change with a factor of $\sqrt{\epsilon_r}$. So, picking the material with a higher permittivity is convenient for the design process. However, picking a material like FR-4 just for its high permittivity can cause other issues. While it has high permittivity, FR-4 also has higher loss compared to other materials, and its permittivity can also be unreliable

at times. Due to these reasons, Rogers RO4003 was chosen as the material. In Table 3.2 a comparison between FR-4 and Rogers RO4003 can be seen.

Table 3.2 Material Properties

Material	ϵ_r	Loss Tangent	Advantages	Disadvantages
FR-4	4.4	0.02	High permittivity Easy to fabricate	High loss Unreliable permittivity
Rogers RO4003	3.55	0.0027	Low loss Easy to fabricate Reliable permittivity	Lower permittivity (Compared to FR-4)

With the material selected, the thickness of the copper layer is decided next for the design process. Rogers RO4003 is manufactured in standard copper thicknesses; 0.008" (0.203mm), 0.012" (0.305mm), 0.016" (0.406mm), 0.020" (0.508mm), 0.032" (0.813mm) and 0.060" (1.524mm). For this thesis, copper thickness of 0.008" (0.203mm) was selected.

3.1.2 Choosing the Design Parameters

For the design of the Rotman Lens, a MATLAB script that takes the design parameters as inputs, calculates the locations of the ports and outputs the geometry of the Rotman Lens was used. This script takes eight inputs, not including the permittivity of the dielectric substrate. These eight input parameters are: the array steering angle, the subtended focal angle, the on-axis focal length, the focal ratio, the expansion factor, the antenna array element spacing, the width of the transmission lines, and the length of the tapers connecting the lens body to the transmission lines.

The steering angle was decided as $\pm 30^\circ$, so this leaves seven other parameters to set. The subtended focal angle, α , is chosen as equal to the scan angle. The focal ratio, β , is chosen as 0.9. The expansion factor, γ , is chosen as 1.1. The antenna array element spacing, whose design will be explained later in this chapter, was selected as 0.56λ , which is approximately 6mm. For the width of the transmission lines, a transmission line calculator tool was used. Using this calculator, the width of the transmission lines was found to be 0.42mm for the chosen substrate.

The on-axis focal length, F , is one of the major parameters that need to be decided. Since it is basically the size of the lens, it cannot be too large. Selecting a smaller F is better for the overall performance of the Rotman Lens, because by making F too large, the path that the signal takes within the lens body becomes longer which

increases the insertion loss of the Rotman Lens. But choosing a small F comes with its own set of problems. If the lens size is too small, the equations that give the coordinates of the ports start to become problematic. Which requires the other parameters to be adjusted once again. Without re-adjusting the other parameters, the largest F was found to be 3.5λ . However, choosing F to be as small as possible would cause issues with the chosen method of coupling between the Rotman Lens and the antenna array, which requires them to be of comparable sizes. For this reason, the on-axis focal length was selected as 3λ .

The final parameter to be set is the lengths of the tapers between the transmission lines and the Rotman Lens. To find the optimum value, a parametric approach was used. By simulating different Rotman Lens's that have different length tapers, the optimum value that give the best S_{11} performance and the least amount of insertion loss was found. For this reason, the tapers, both at the array ports and the beam ports, were selected to be 2λ [17] [18].

By giving these inputs to the MATLAB script, as seen in Table 3.3, the lens geometry seen in Figure 3.1 was obtained.

Table 3.3 Selected Design Parameters

Center frequency	28GHz
Number of beam ports	5
Number of array ports	6
Steering angle	$\pm 30^\circ$
Focal angle	30°
Focal ratio	0.9
Expansion factor	1.1
Array element spacing	0.56λ
Transmission line width	0.42mm
On-axis focal length	3λ
Taper length	2λ

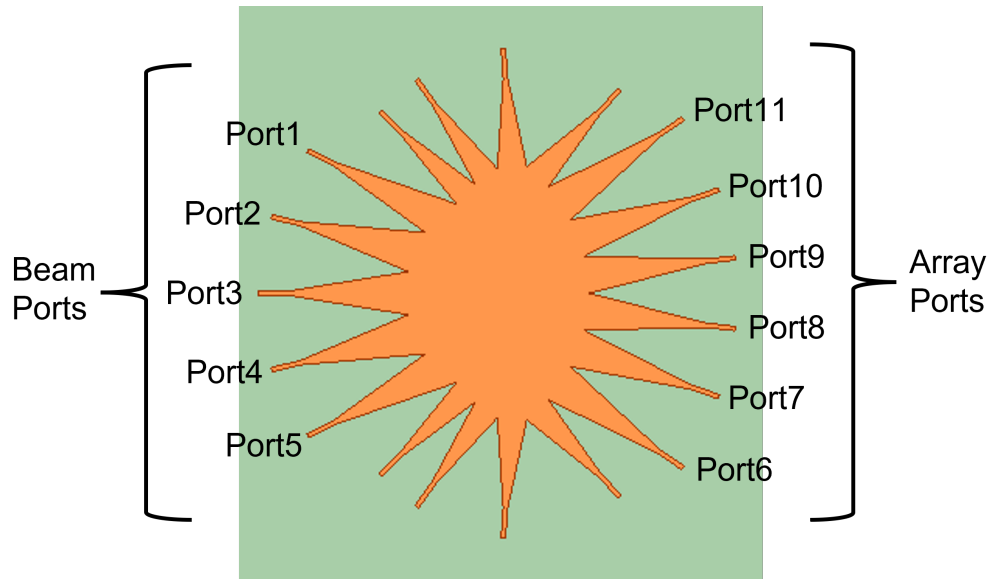


Figure 3.1 Lens Geometry

3.2 Simulation Results of the Rotman Lens

Using another MATLAB script, the lens geometry was mapped to an HFSS project to be simulated. In the simulation setup, all the ports were excited by using 50Ω . For this part of the design process, the dummy ports were also assigned excitations to see their effect on the performance of the lens. In this section, the S-Parameters of the simulated design will be presented.

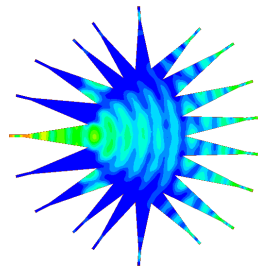
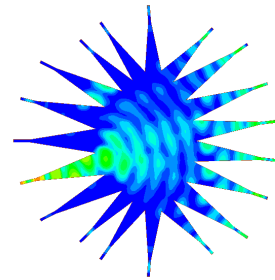
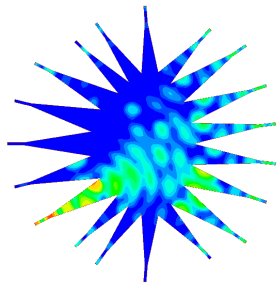


Figure 3.2 Signals

3.2.1 Return Loss

The return losses of both the beam ports and the array ports were looked into. S11 of both the beam ports and the array ports vs frequency can be seen below in Figures 3.3 and 3.4. The S11 plots show that the return loss of all the ports is below -10dB in the frequency of interest.

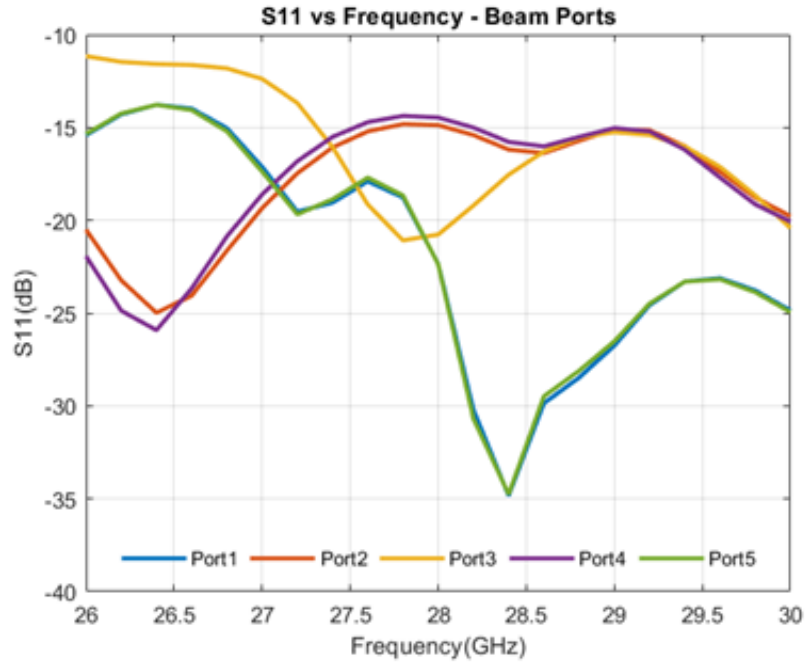


Figure 3.3 S11 of the Beam Ports

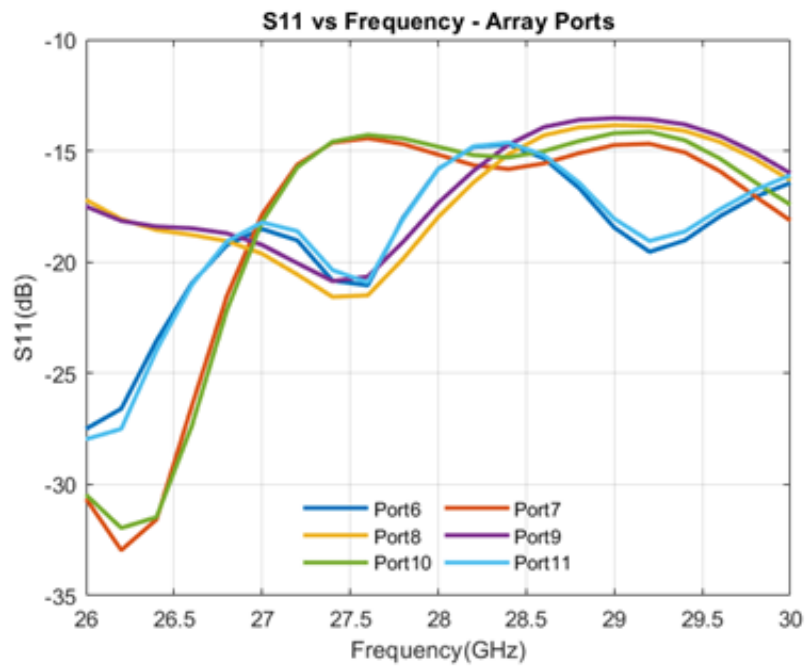


Figure 3.4 S11 of the Array Ports

3.2.2 Isolation

The coupling between adjacent ports can be problematic. Especially since the port centers are relatively close to each other, and reflections happen within the lens body. Which is why the isolations between ports should also be observed when going forwards with the design of a Rotman Lens.

In the Figures 3.5 and 3.6 below, the isolation between the beam ports and array ports are plotted. The plots show that the isolations between the beam ports are all below -15dB, and while the isolations between the array ports are higher towards the lower end of the band of interest, it never goes above -12dB, so the isolation values are always within acceptable levels.

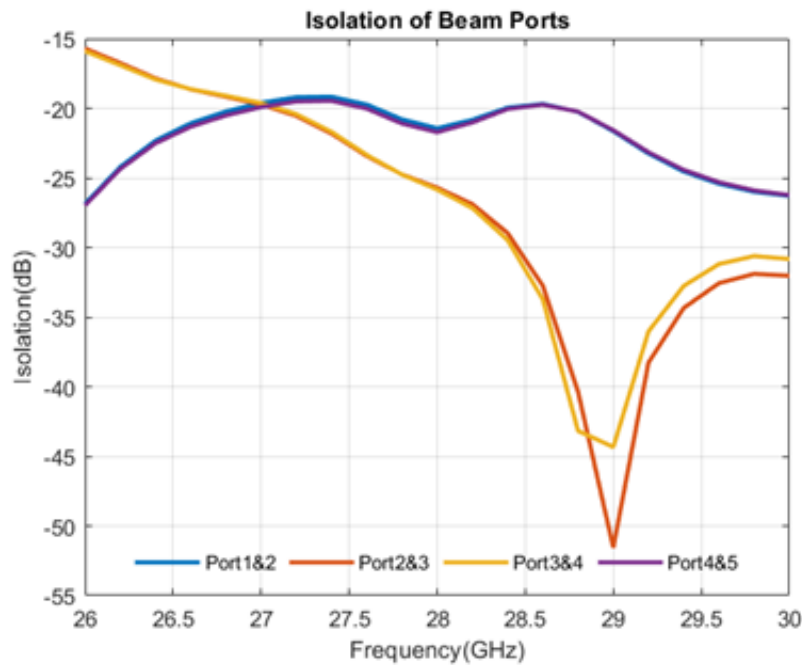


Figure 3.5 Isolation Values Between the Beam Ports

3.2.3 Phase Adjustments

With the geometry of the Rotman Lens decided upon and the S-Parameters checked, the phase performance should be inspected next. To do this, the design was exported to ADS and simulated there, since designing the transmission lines to adjust the phase differences between the array ports will be both easier and faster using the tuning tool of ADS.

The S-Parameter file of the design was exported from HFSS, and the simulation setup was done on ADS. Transmission lines were added to the beam and the array ports. The widths of these transmission lines are 0.42mm, to be matched to 50Ω.

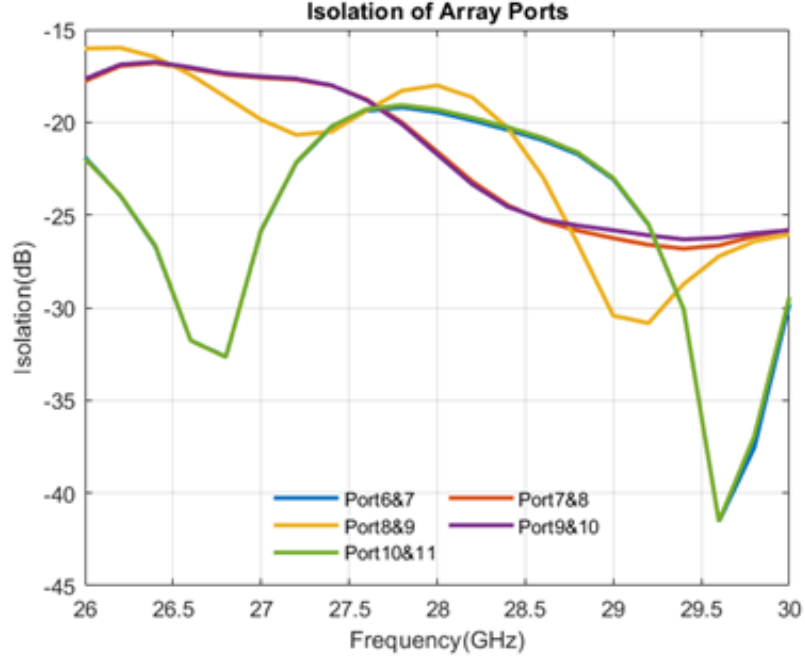


Figure 3.6 Isolation Values Between the Array Ports

For the antenna array to radiate the beams in the angles that are wanted, the phase differences between adjacent array ports need to be adjusted. Upon inspection of the effects of the transmission lines on the phase differences between the array ports, it was realized that the transmission lines added to the beam ports of the Rotman Lens affect the phase differences between all six array ports, which was the expected outcome. Using the following equation, the lengths of the transmission lines were adjusted so that the phase differences were as wanted.

$$\Delta\Phi = 2\pi \frac{d \sin \theta}{\lambda}, \quad (3.1)$$

In this equation, $\Delta\Phi$ is the phase difference between adjacent array ports, d is the distance between the antenna arrays, θ is the radiation angle and λ is the wavelength.

3.3 Simulation Results of the Antenna Array

After the Rotman Lens was designed and the necessary phase corrections were done, the design of the antenna array was finalized. Since the number of array ports on the Rotman Lens was six, an array consisting of six elements was designed [19].

The antenna elements were designed to be centered at 28GHz, with as little sidelobe generation as possible, while also having as much gain as possible. For this, an array that consists of elliptical elements was used. In each segment of the array ten

antenna elements were used, to increase the gain of the system as much as possible. The sizes of each antenna element were further optimized to achieve the smallest sidelobe levels possible. To further lower the sidelobe levels, there is a distance of $\lambda/4$ between each element of the individual arrays. With these adjustments, a gain of 13.7dBi was reached, with side lobe levels lower than 3dBi. The final design of the array can be seen below in Figure 3.7, and the results of the simulations can be seen in Figures 3.8 and 3.9.

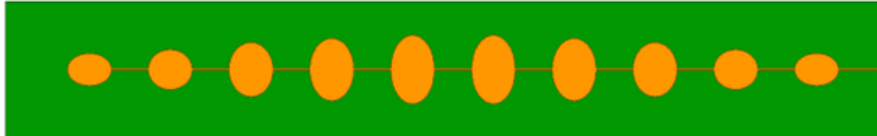


Figure 3.7 View of the 1x10 Antenna Array

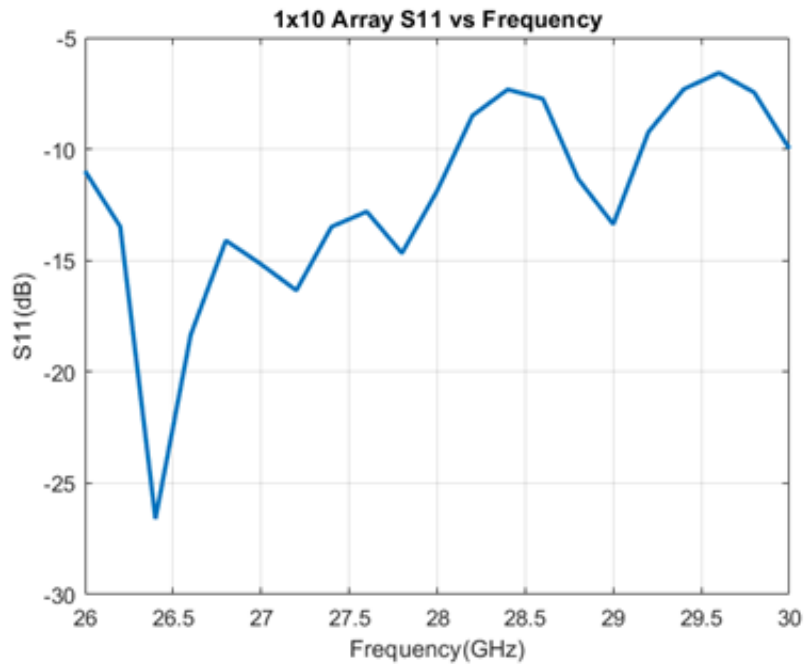


Figure 3.8 S11 of the 1x10 Antenna Array

3.4 Rotman Lens and Antenna Array Connections

After the design of the antenna array was completed, the next step was to design the transmission lines that would connect the array ports of the Rotman Lens to the antenna array, and the transmission lines that would connect the beam ports of the Rotman Lens to the connectors on the edge of the board.

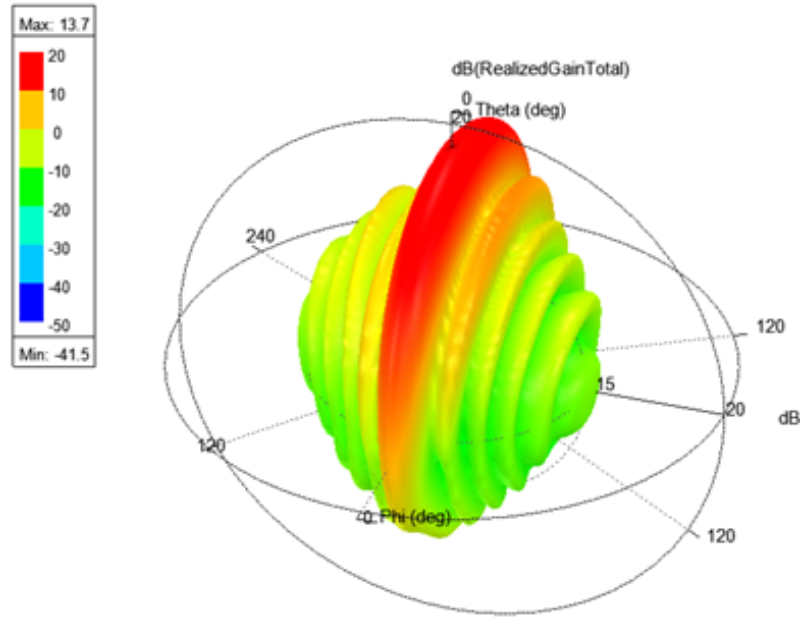


Figure 3.9 3D View of the Beam Generated at 28GHz

After the initial design of the Rotman Lens, the necessary phase adjustments were already made. Which means that one of the things that needed to be kept in mind during the design process of the transmission lines is that they should all have the same lengths, so that no unwanted phase changes would occur at the outputs.

The other detail to keep in mind was where the transmission lines would end. The antenna array was designed such that the distance between them was 0.56λ , which is equal to 6mm. The transmission lines between the array ports and the antenna array also need to end with the same distance between them. For the lines between the beam ports and the connectors, they need to end on the same line, so that the connectors can be attached to the edge of the board.

The transmission lines were also kept to have the same electrical lengths. In the conventional Rotman Lens design, this is also done. However, since the lengths of the transmission lines at the array ports of the lens are what affects the phase differences between adjacent array ports. So, their lengths are important to keep the phase differences at the wanted values.

In this design, the transmission lines that connect the beam ports to the connectors were also designed to have the same electrical lengths. By having them at the same lengths, the input signals that go into the lens cavity are kept in-phase with each other. This allows for the signals coming from different ports to be added to each other. By adding the signals together, new phase differences were achieved, and extra beams were generated. In the conventional Rotman Lens design, the number

of beams generated are equal to the number of beam ports on the lens. However, by designing the transmission lines in such ways, seven beams can be generated from five beam ports.

To minimize the area of the design, the transmission lines were designed to be curved while also having the same length. The final design of the Rotman Lens with the transmission lines attached can be seen in Figure 3.10.

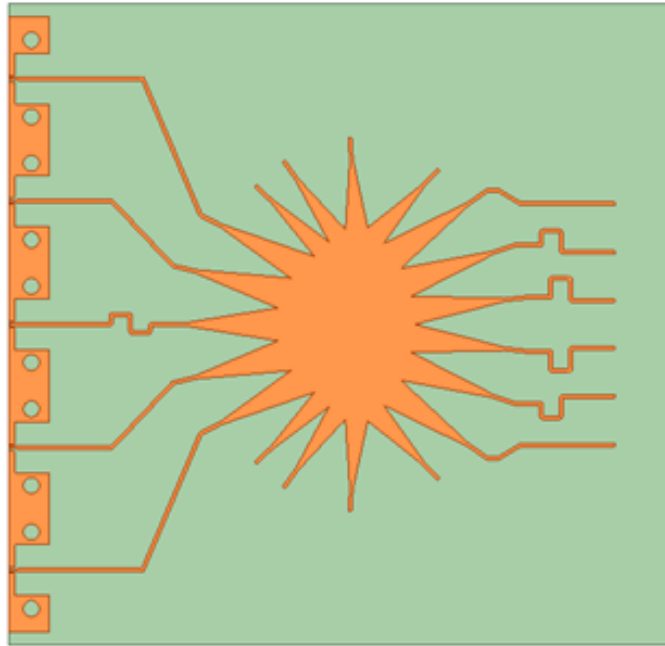


Figure 3.10 View of the Rotman Lens with the Transmission Lines Added

The changes made to the design of the dummy ports will be explained later on in this chapter.

3.5 Design of the Slot Coupling

Conventional Rotman Lens design utilizes transmission lines or coaxial cables to connect the array ports of the Rotman Lens to the antenna array. However, in cases where the size of the array is large, these methods would make the footprint of the design too big. For this reason, an approach that would not make the size of the designed board too large while also not affecting the amplitude performance of the beams was selected [20].

To connect the Rotman Lens and the antenna array, slot coupling was used. Slots were opened on the ground plane of the design and the feeds of the antenna and the transmission lines coming out of the array ports were aligned. Since there are now openings in the ground plane, the signal can couple through the substrate layer.

The size and position of the slot is what affects the insertion loss through it. Initially, a slot that has a length of $\lambda/4$ was opened. The width of the slots was the same as the transmission lines, 0.42mm. Parametric simulations of the slot sizes were done, it was found that the slots have the best insertion loss performance at these sizes. The position of the slots also affects the insertion loss. The simulations were run with the slot at different position on the transmission lines, and it was found that while the position does not have too big of an effect on the insertion loss, the insertion loss has the least amount of deviation when the slot is positioned 1mm away from the end of the transmission line.

The simulation results and the slots can be seen in Figures 3.11-3.14.

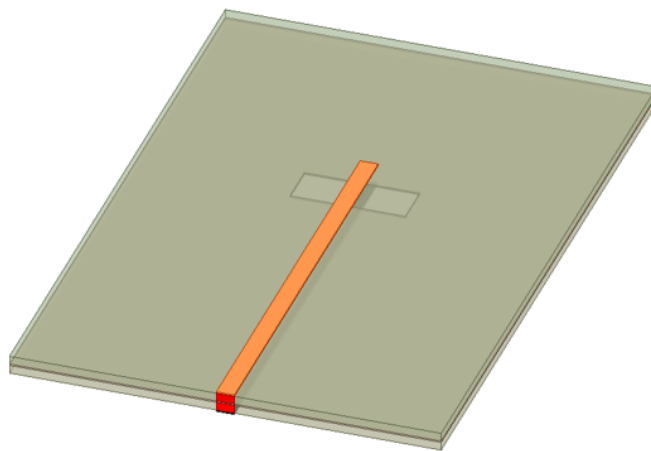


Figure 3.11 Top View of the Slots

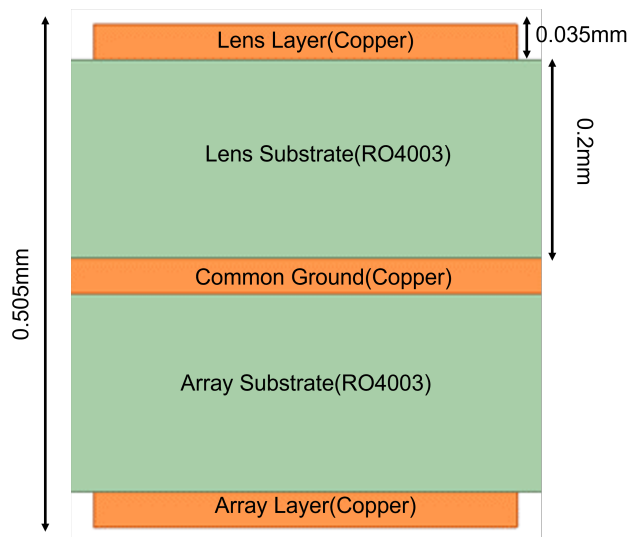


Figure 3.12 Side View of the Layers

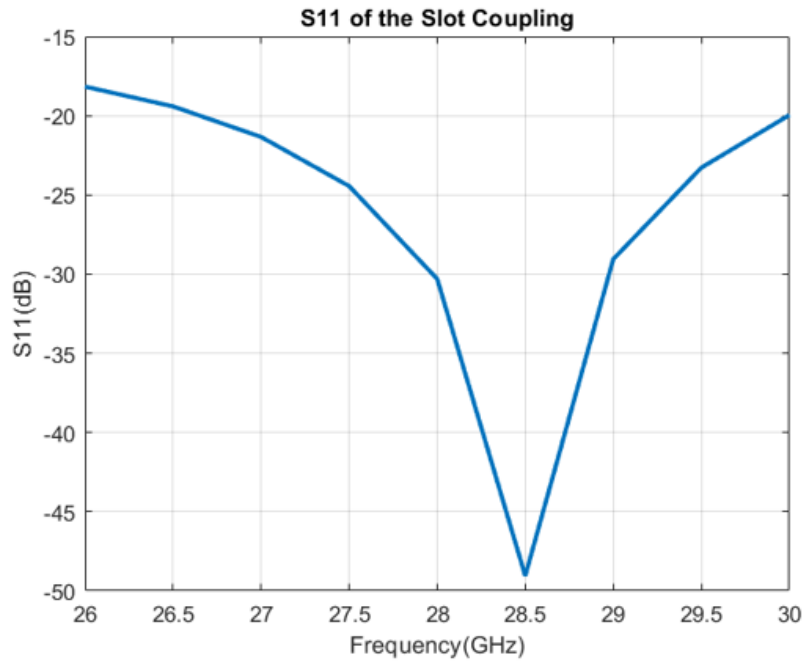


Figure 3.13 Return Loss of the Slot Coupling

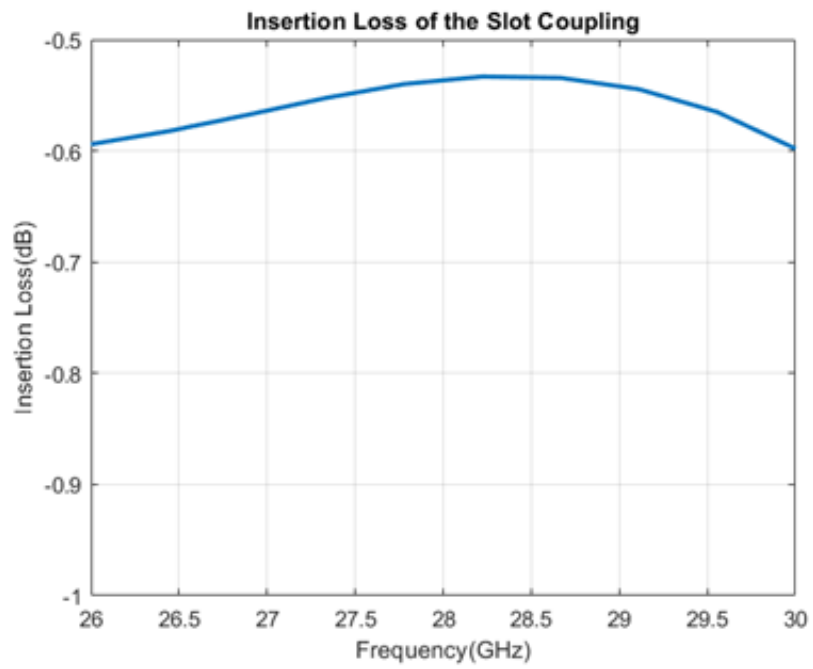


Figure 3.14 Insertion Loss of the Slot Coupling

3.6 Design of the Dummy Ports

With the Rotman Lens and the antenna array coupled, the focus of the design was shifted towards the dummy ports, the ports that are on the sides of the Rotman Lens.

While the beam and array contours are designed based on defined equations, the sidewalls are not. The signal coming from the beam ports can be reflected on these sidewalls, making the signal go through a secondary unwanted path and causing unwanted phase differences in the array ports.

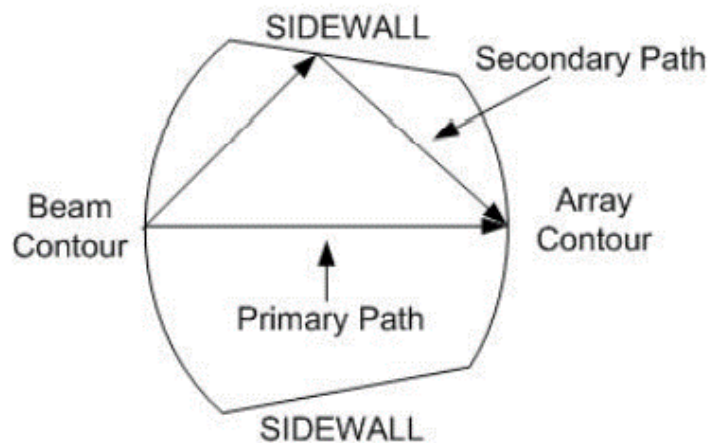


Figure 3.15 Reflections From the Sidewall

In the conventional microstrip Rotman Lens design, dummy ports are used to deal with the problems that the sidewalls present. The dummy ports are connected to 50Ω resistors, so that if the signal goes through them the reflections within the lens cavity can be minimized. However, using this method can cause another problem. If the dummy ports are connected to 50Ω resistors, the resistors will need to be connected to the ground plane, which will require vias to be opened through the substrate, increasing the cost of the design.

In this thesis, a design approach based on parallel resistor networks was used. The resistances that are seen at the ends of the dummy ports were found using the simulation data of the Rotman Lens. Afterwards, quarter wave transformations was used on these ports and the resistances were transformed to 200Ω . With the resistance values at 200Ω , the transmission lines were connected together, creating a network of four parallel 200Ω resistors which makes the equivalent resistance value 50Ω .



Figure 3.16 Conventional Dummy Ports with Connectors Attached

Originally, the goal was to use these parallel transmission lines to reduce the required resistor/connector number from eight, four on each side of the lens, to two, one on each side.

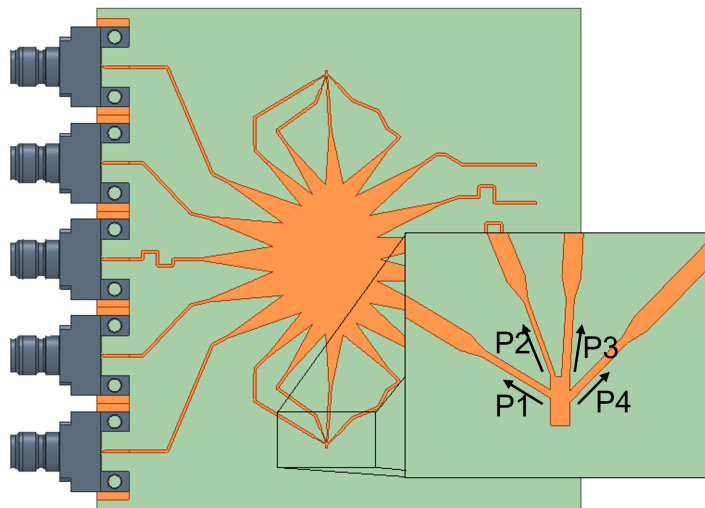


Figure 3.17 The Dummy Ports Connected Together

However, since there are an even number of dummy ports on each side, these connectors could also be omitted. After the quarter wave transformations, the ports were all observed to be matched to 200Ω . Which means that connecting these ports in pairs would essentially create two 200Ω resistances in parallel, making them equal to 100Ω . Both of these pairs were matched to 100Ω and consequently wanted to be terminated with 100Ω . Since they were both matched to 100Ω , they could act as termination to each other.

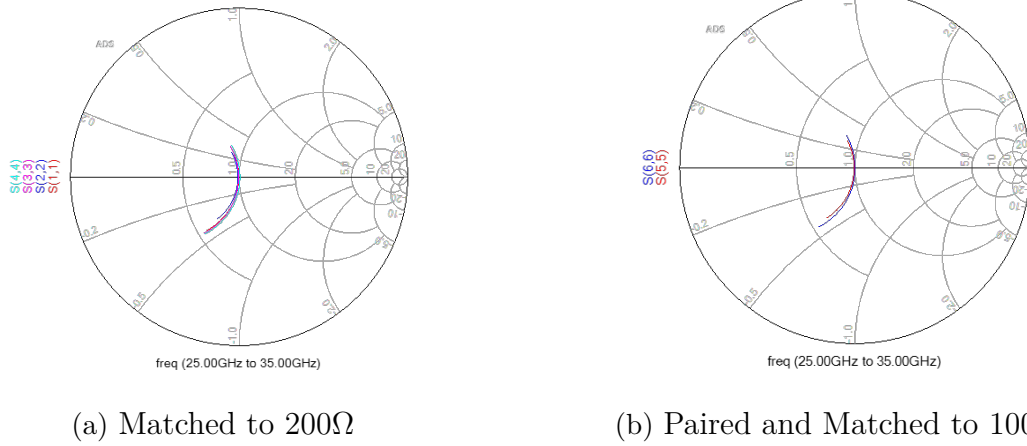


Figure 3.18 Reflection Coefficients of the Dummy Ports

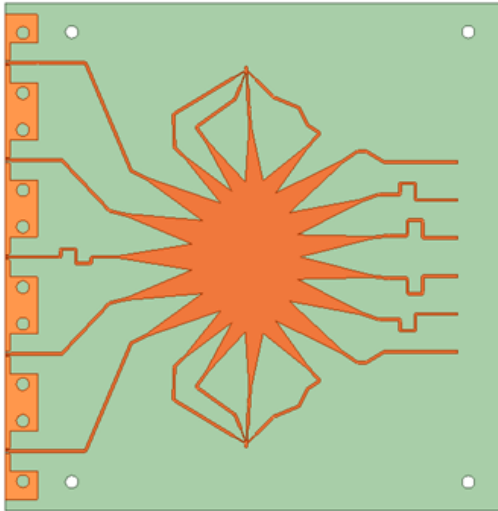
Making the dummy port connections in such a way made it so that the connectors could be removed completely. So, manipulating the resistance values and matching requirements of the dummy ports, the number of required dummy port connectors were reduced to zero.

3.7 Implemented Design

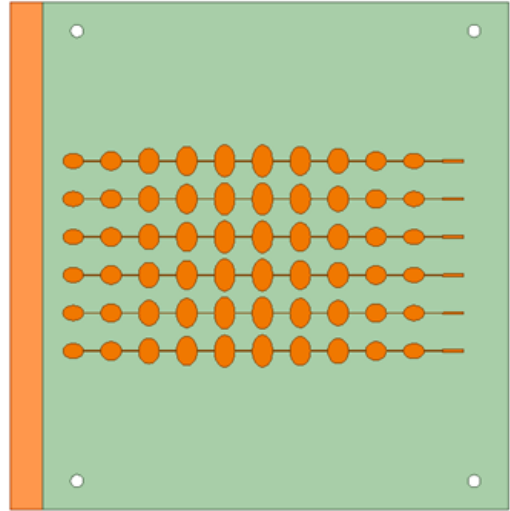
The implemented design of the Rotman Lens can be seen in Figure 3.19. The lens has five beam ports on the left side and six array ports on the right side of the figure. With the dummy ports on each side of the Rotman Lens, there are a total of 19 ports. The array ports are coupled to the antenna array on the backside of the board through the slots opened in the ground plane in between. The slots opened in the ground plane can be seen in Figure 3.20. The final size of the board is 80mm by 78.7mm. The lens was designed to scan up to $\pm 30^\circ$ and with five beam ports, can generate five beams at $\pm 30^\circ$, $\pm 15^\circ$ and 0° . Since the transmission lines were designed to have the same lengths, the three inputs in the middle can be fed together creating two more beams at $\pm 7^\circ$.

3.7.1 Simulation Results of the Implemented Design

After the design of the board was finalized, the final simulations were run. The results of these simulations will be presented in this section. The results that were obtained by simulating the parts of the design individually were also checked when they were connected together.



(a) The Complete Rotman Lens



(b) The 6x10 Array

Figure 3.19 Complete Design

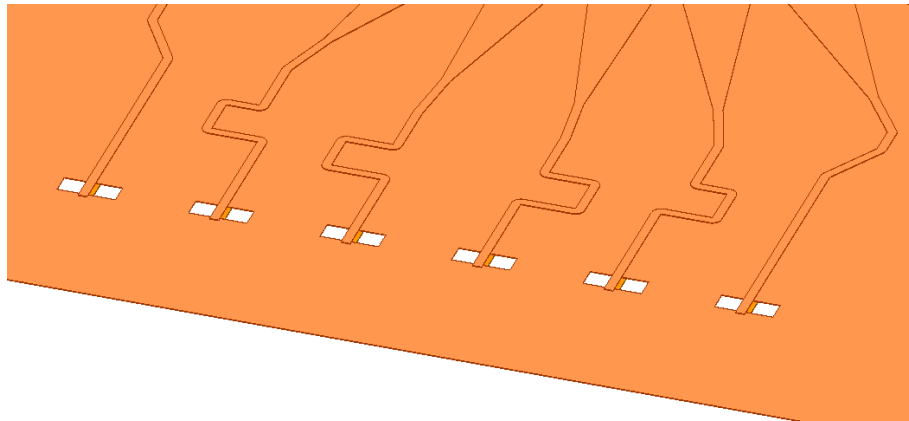


Figure 3.20 Slots Opened in the Ground Layer

The important results that will be reported are the return loss of the Rotman Lens, the isolations between the ports, and the beams that were generated. For the isolations between ports, only the values for the beam ports that are next to are presented. The plots of these results can be seen in Figures 3.21-3.23.

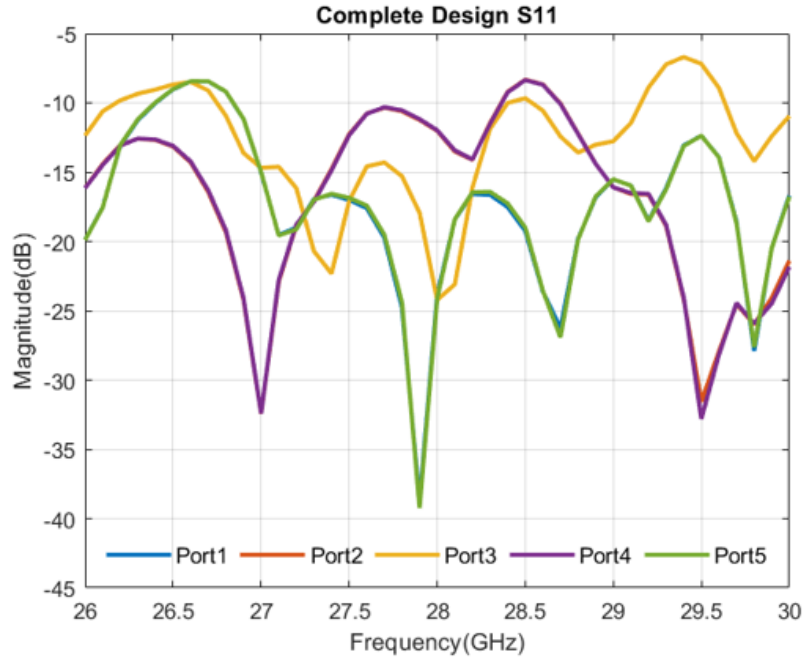


Figure 3.21 Return Loss of the Final Design

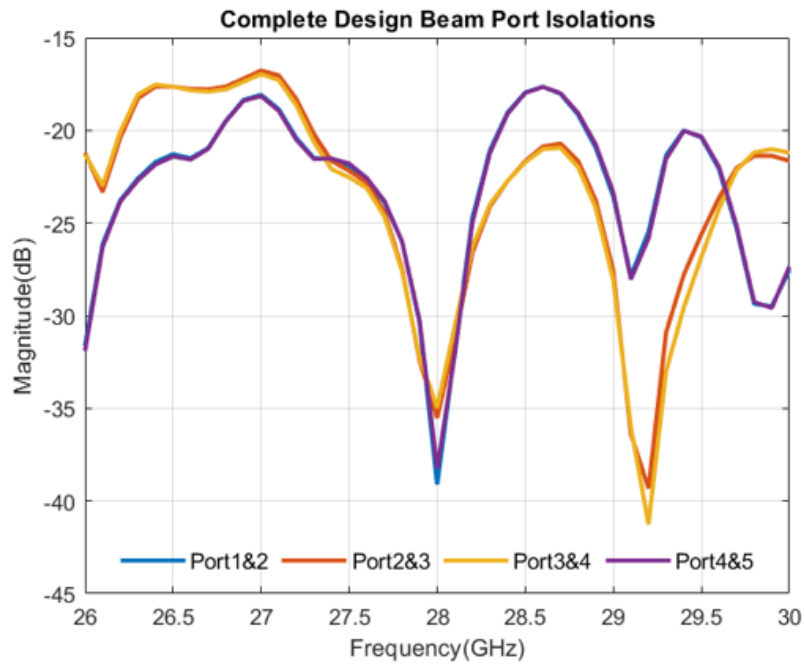


Figure 3.22 Isolation Values of the Final Design

In Figure 3.23, all of the beams that can be generated at 28GHz are shown. From this figure, it can be seen that the sidelobe levels are low compared to the beam center. The 3dB beamwidths can also be determined from this figure. 3dB beamwidth values can be seen in Table 3.4. The 3dB beamwidth becomes important when there is a change in which input is being fed. For the transition between beams to be smooth, 3dB beamwidth of adjacent inputs should be crossing over each other.

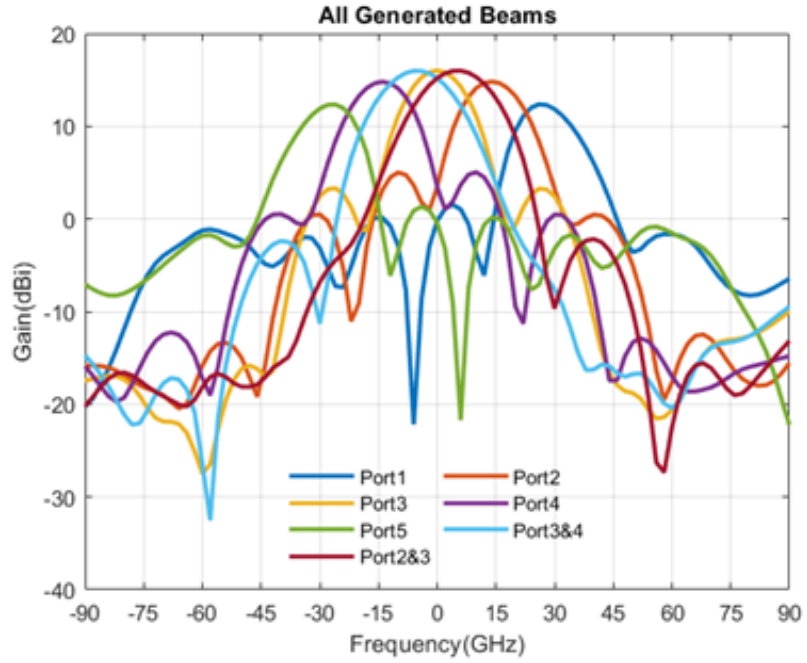


Figure 3.23 All Generated Beams

Table 3.4 3dB Beamwidth at 28GHz

Beam Port	3dB Beamwidth
Port1(+28°)	16
Port2(+14°)	16
Port2&3(+6°)	20
Port3(0°)	16
Port3&4(-6°)	20
Port4(-14°)	16
Port5(-28°)	16

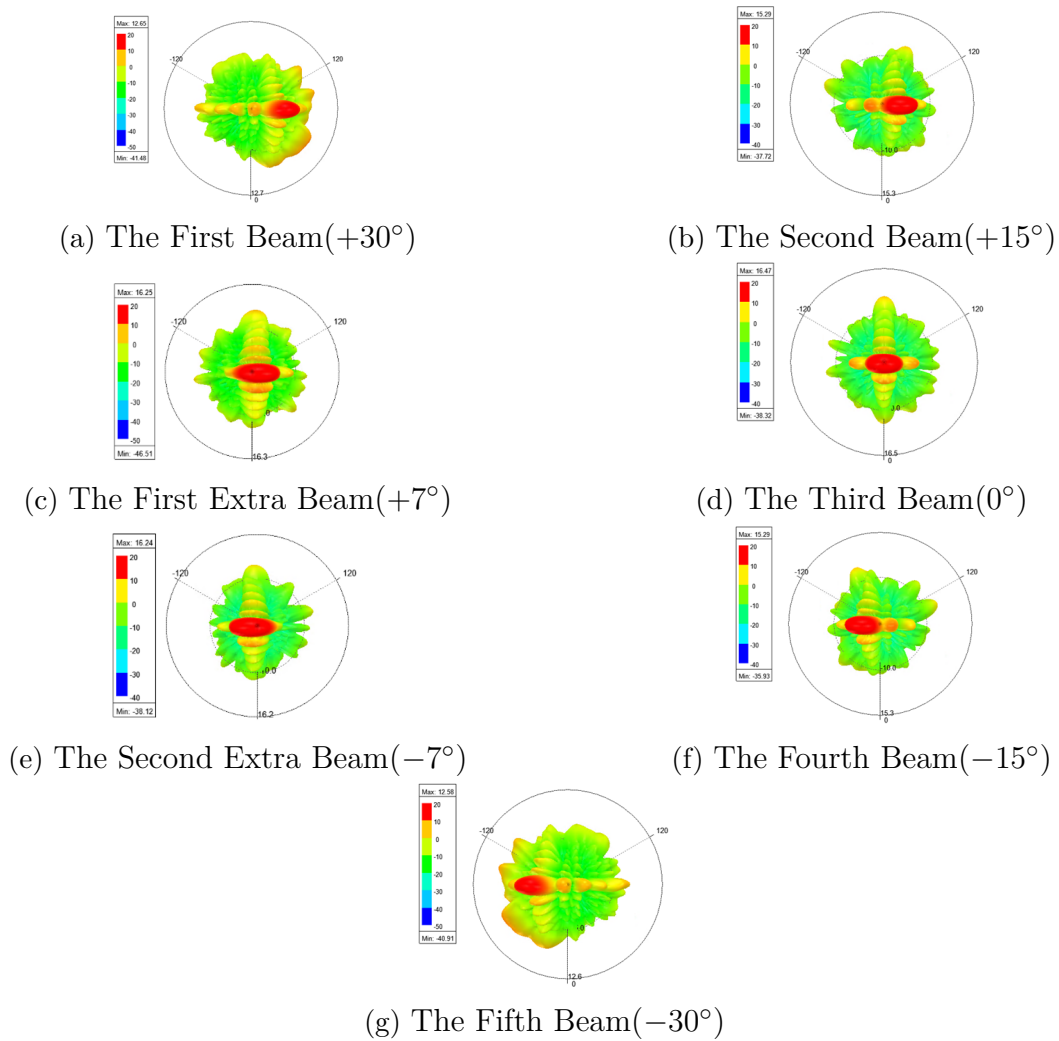


Figure 3.24 3D Views of the Generated Beams

Table 3.5 First Sidelobe Levels at 28GHz

Scan Angle	First Sidelobe Level
+28°	-10.7584
+14°	-9.8093
+6°	-18.1886
0°	-12.7005
-6°	-18.3668
-14°	-9.757
-28°	-10.9729

Chapter 4

MEASUREMENT RESULTS

In the previous chapter, the design process and the simulation results of the Rotman Lens was shown. The final design was then implemented, and several measurements were taken. In this chapter, the results of these measurements will be presented, and the performance of the implemented design will be compared to those of the simulated design.

4.1 Production of the Board

The final design of the Rotman Lens and the antenna array were manufactured on Rogers RO4003. Since the board was design to be three layered, the two designs were manufactured separately and were put together afterwards. The design was assembled using three different methods: by using glue, by using screws to hold the boards together, and by using epoxy to glue the boards. The effect these methods had on the measurement results will be discussed further in the chapter. After the boards were attached to each other, the connectors were screwed on. For the connectors, Southwest Microwaves 1092-01A-6 was used. The connectors were attached carefully since the pin may move and affect the performance of the design. The fabricated boards can be seen in Figure 4.1.

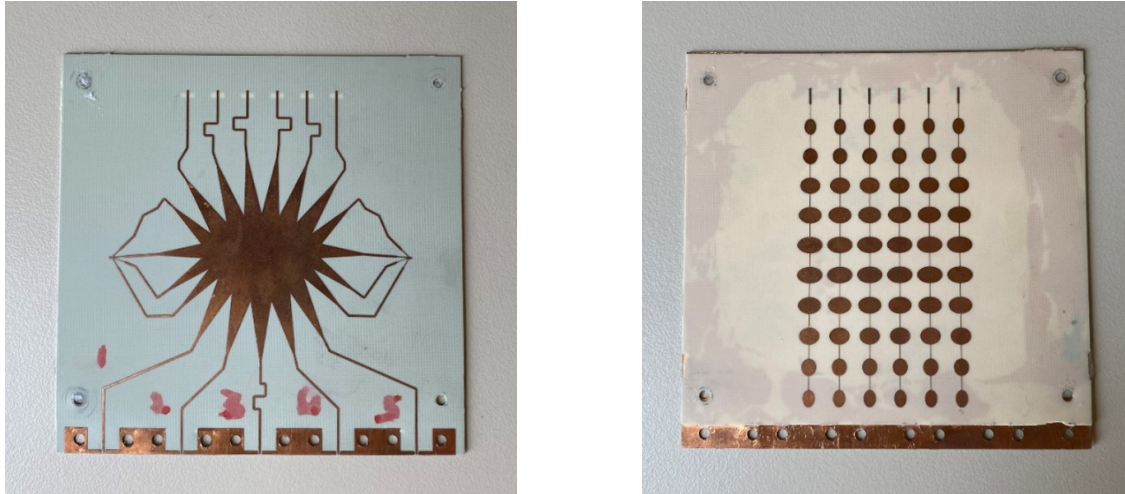


Figure 4.1 Fabricated Array and Rotman Lens

4.2 S-Parameter Measurements

After the boards were assembled, the S-Parameters were the first thing that was checked. This way, the reflections of the ports were determined and if there was a problem with them, it could be found and solved before doing far field measurements. The S-Parameter measurements were done using Agilent PNA 5245A vector network analyzer. During the measurements, the ports that were not being measured were terminated using 50Ω connectors, to prevent any unwanted reflections. In this section, the results of the S-Parameter measurements of the three boards previously mentioned will be presented.

4.2.1 Glue to Hold the Boards Together

The first design that was measured was the one where the two boards were glued together, using Adhетron EP2669. The reflection coefficients of this board can be seen in Figure 4.2.

Looking at the reflection coefficient measurements, it can be seen that the S11 values of all the ports are below -10dB within the bandwidth of interest. Compared to the simulation results, the performance of the reflection coefficients seems better than expected.

After the reflection coefficients were measured, the isolations between the beam ports were also measured. This was done so that the couplings between the input ports can be seen and their effect on the performance can be checked. The measured isolations can be seen in Figure 4.3.

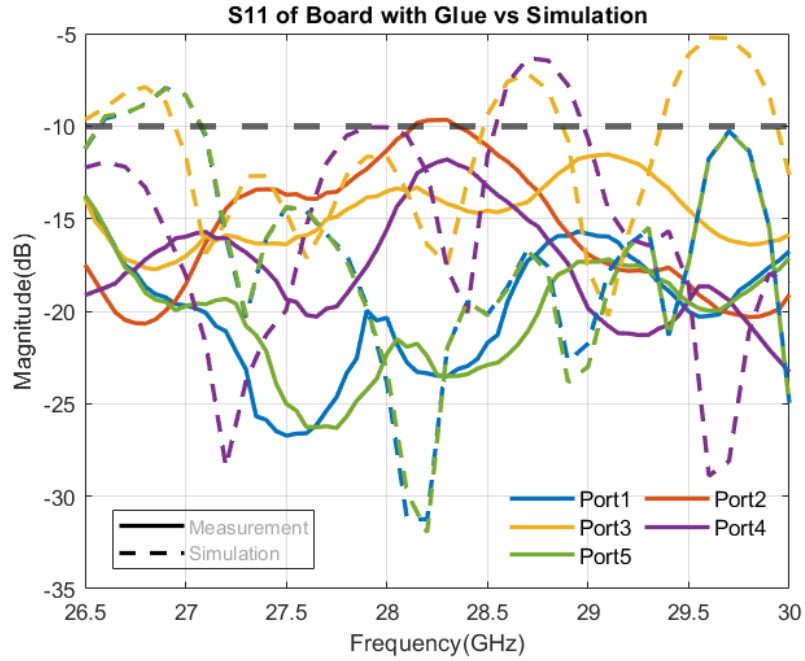


Figure 4.2 Reflection Coefficients of Board with Glue vs Simulation

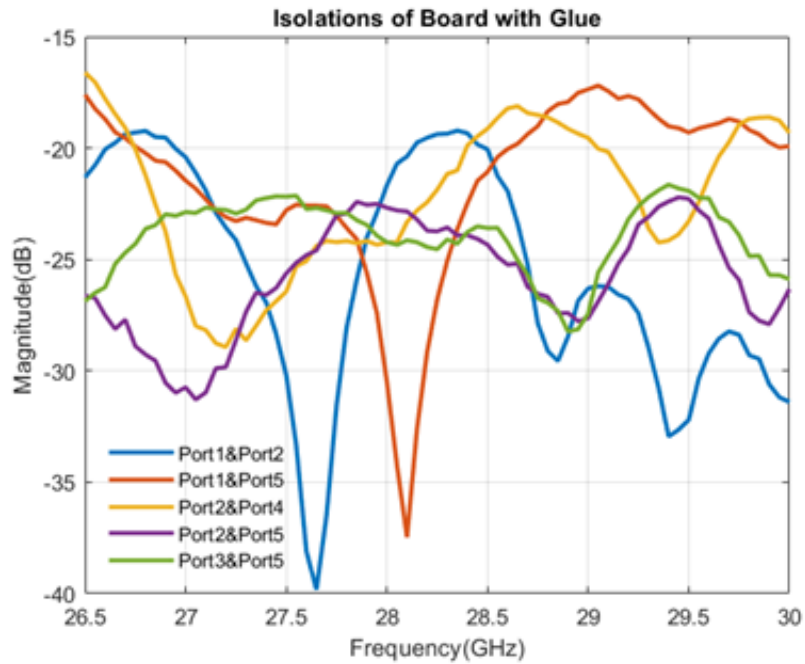


Figure 4.3 Measured Isolation Values of Board with Glue

As seen in the measurement results, the couplings between the boards are all below -15dB, so the beam ports shouldn't have any noticeable effect on each other.

Since the Rotman Lens and the array were glued together, the connectors cannot be attached to the array ports, so their S-Parameter performances cannot be checked. However, since the reflection coefficients and the couplings between the beam ports

are all within expected values and similar to the simulation results, it is safe to assume that the array ports will also behave similarly

After the S-Parameters were checked, the far field measurements were performed. The results of these measurements will be shown later on in the chapter.

4.2.2 Screws to Hold the Boards Together

After the measurements for the board assembled using glue was completed, the measurements of the board that was assembled using screws were taken. For this board, the holes that were opened for alignment were used as screw holes. The Rotman Lens and the array were screwed together on the four corners of the board and were then measured.

The measurements procedure was similar to that of the board that was glued. First the S-Parameters were measured and afterwards the far field measurements were completed. For the S-Parameters, the reflection coefficients of the beam ports were checked.

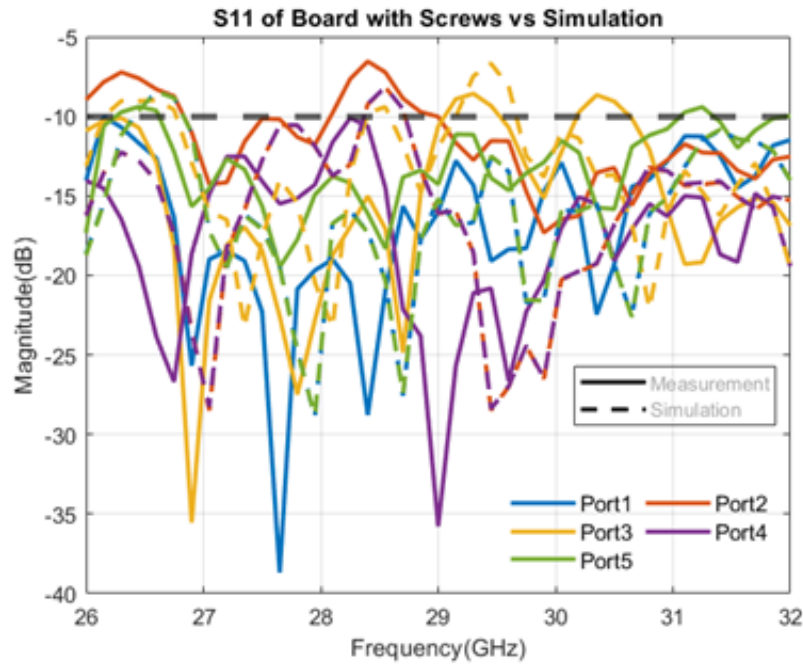


Figure 4.4 Reflection Coefficients of Board with Screws vs Simulation

Since the isolation values of the previous board that was assembled using glue were good, they were not checked for this board. The only thing that was different in this measurement setup was the way that the boards were assembled, which does not have a major impact on the coupling between the beam ports. For this reason, the isolation values should have similar values to the previous case.

After the S-Parameters were checked, the far field measurements were done. The results of the far field measurements will be presented later in this chapter.

4.2.3 Epoxy to Hold the Boards Together

The third board that was measured was the case when an epoxy was used to glue the boards together. In this case, a two-part epoxy was used on the edges of the boards to glue them together. After the epoxy was applied, the connectors were once again attached, and the relevant measurements were done.

The measurements done are the same as before. The S-Parameters were checked and seeing that there were once again no reflections in the beam ports, the far field measurements were done.

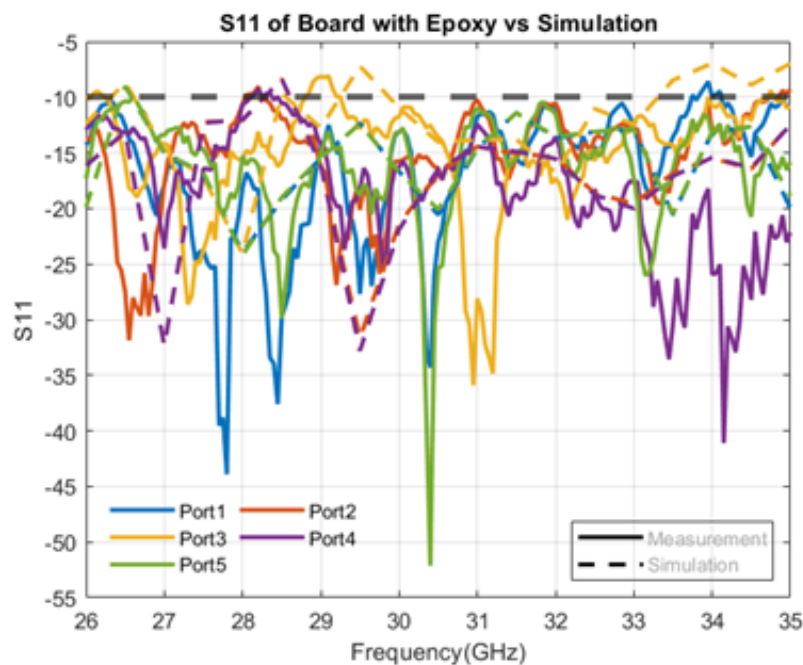


Figure 4.5 Reflection Coefficients of Board with Epoxy vs Simulation

Similar to the previous case, the isolations were not checked again. For the same reason as before, only changing the way the boards were assembled doesn't have a significant effect on the couplings between the adjacent ports.

After the completion of the S-Parameter measurements, the far field measurements were done. The results of the far field measurements will be shown later in this chapter.

4.3 Far Field Measurements

After the S-Parameters of the boards were measured and were observed to be within acceptable levels, the boards were taken to the anechoic chamber within Sabanci University Nanotechnology Center (SUNUM) for far-field measurements. The measurement setup was done so that there is a distance of 1.7m between the device under test (DUT), and the receiving horn antenna. The boards were all individually measured at different frequencies. In this section, the data obtained from these measurements will be presented, and compared to the results obtained from the simulations. For the beams that were generated by feeding adjacent beam ports, a Sigtek SP70203 was used.

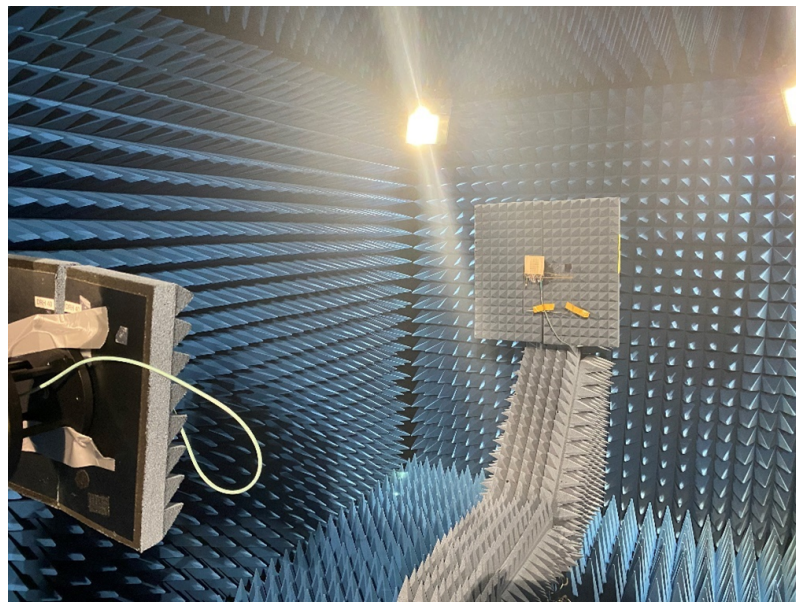
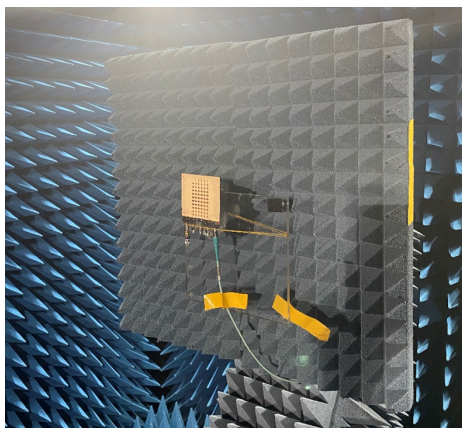
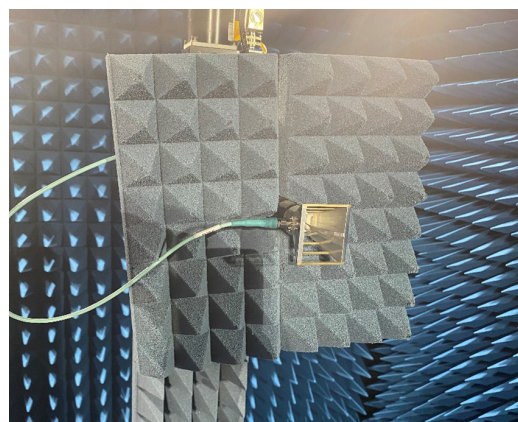


Figure 4.6 The Measurement Setup



(a) The DUT



(b) The Receiving Antenna

Figure 4.7 Devices Used for Far Field Measurements

4.3.1 Glue to Hold the Boards Together

After the S-Parameter measurements of the boards that were glued together were completed, it was taken to the anechoic chamber for far-field measurements. The DUT was setup, and the measurements were completed. The resulting beams from the measurement can be seen in Figure 4.8.

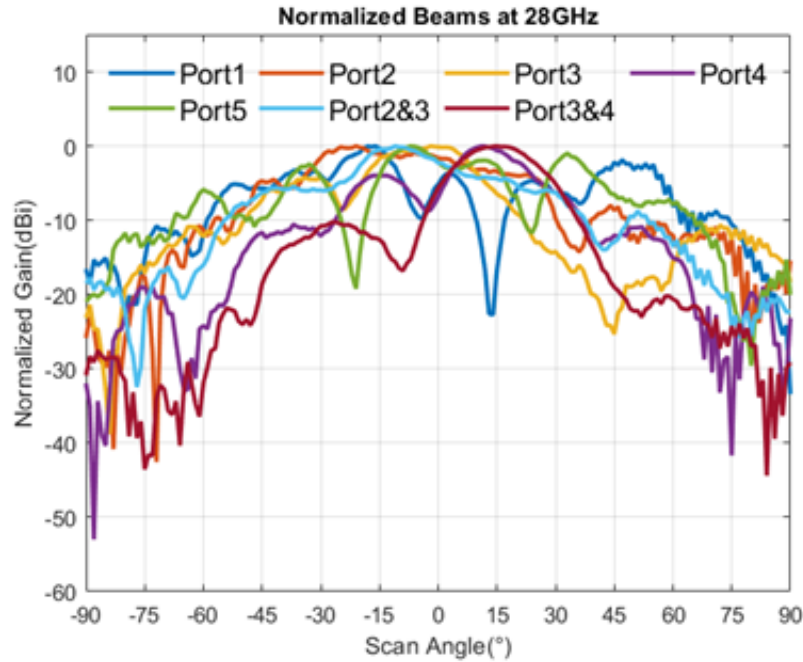


Figure 4.8 Normalized Beams at 28GHz

After the measured beams were plotted, it was realized that the beams were formed at the wrong angles. After this realization, the maximum values of the beams were plotted. This was done so that if there was a shift in the center frequency of the it could be observed, and the cause of the problem could be found. The maximum realized gain plot can be seen in Figure 4.9.

After the maximum realized gain was plotted, it was observed that the gain values of the measured board were increasing with frequency. Looking at the gain vs frequency graph, it was decided that the antenna array was not working as intended. Since the measured S-Parameters were in line with the simulations, the Rotman Lens' performance does not look to be the issue here.

Since the array was decided to be the factor that was disrupting the performance of the board, the differences between simulations and the fabricated board were inspected. In this case, there were two differences. The first one is that the connectors were not implemented in the simulations. They could have been changing the phases of the signals going into the device. However, these connectors were used in previous

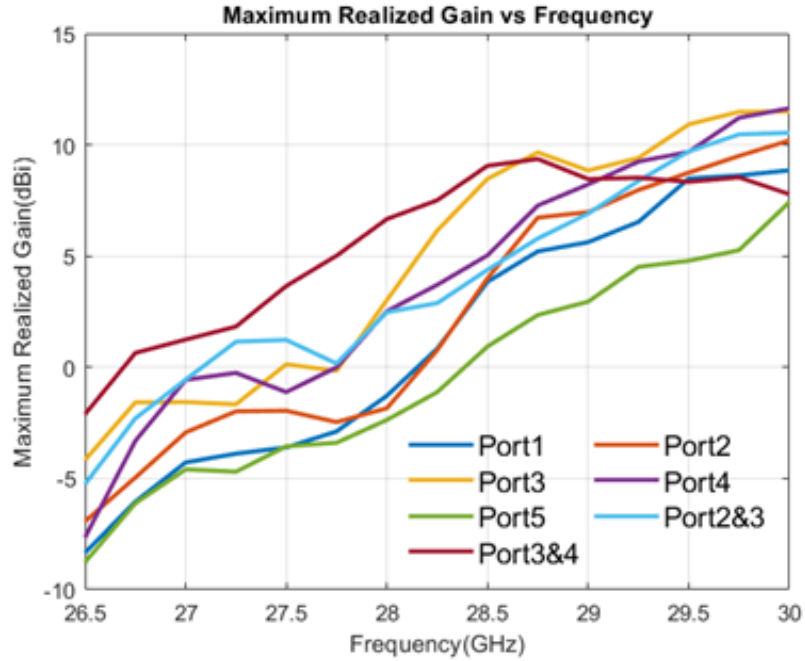


Figure 4.9 Maximum Realized Gain vs Frequency

measurements with no impact on the results. So, the cause of these measurement results must be something else.

The other difference from the simulations was the way that the board was assembled. The glue between the array and the Rotman Lens was not in the simulation. This was the cause of the frequency shift and the gain loss seen in the measurement results. The glue between the layers was affecting the grounding of the antenna array. The glue between the layers was removed and new measurements were performed.

4.3.2 Screws to Hold the Boards Together

After the necessary S-Parameter measurements were completed, the DUT was setup in the anechoic chamber to be measured. Unlike the previous measurements, this time there was not anything between the array and the ground layer, so the grounding problem was expected to be solved. The results of the measurements can be seen in Figure 4.10.

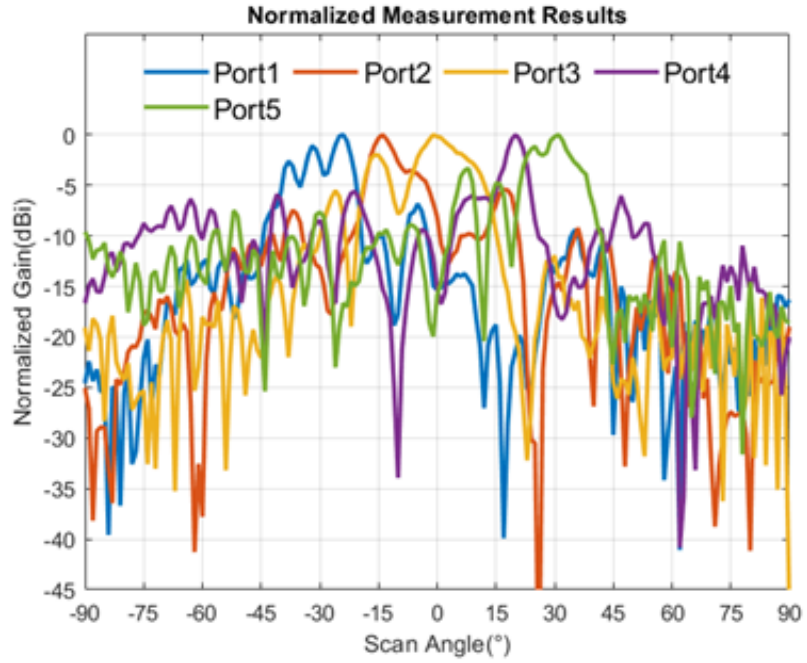


Figure 4.10 Normalized Beams at 28GHz

The beams generated at 28GHz still have the same problem of not having high gain as the previous DUT. Looking at the gain vs frequency graph from the previous measurements, the gain was determined to be higher as the frequency gets higher. The beams generated at 35GHz can be seen below in Figure 4.11.

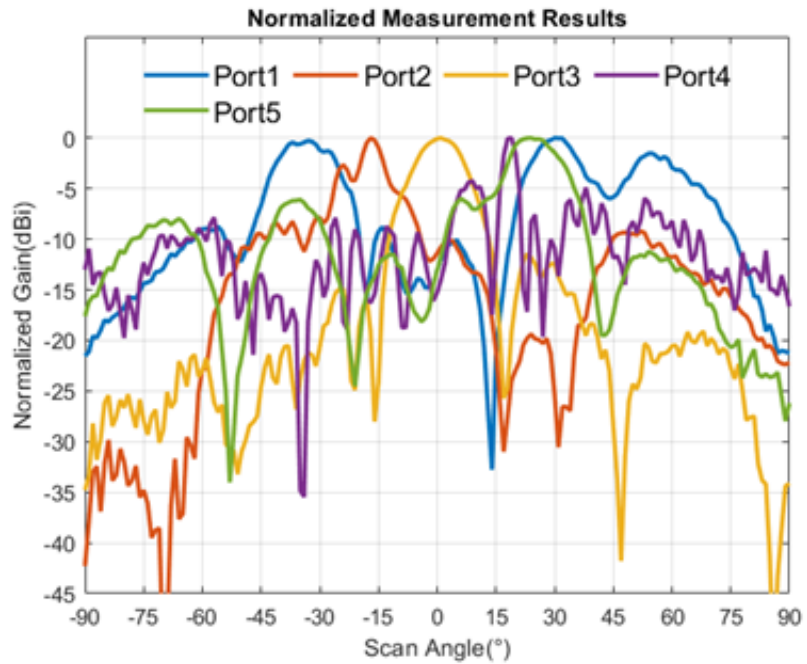


Figure 4.11 Normalized Beams at 35GHz

The gain values at 35GHz were better, but the shapes of the beams were problematic. After looking at the assembled board, it was realized that there was an air layer of 0.1mm left between the ground layer and the antenna array. Similar to the glue used before, this air layer was affecting the grounding of the antenna array.

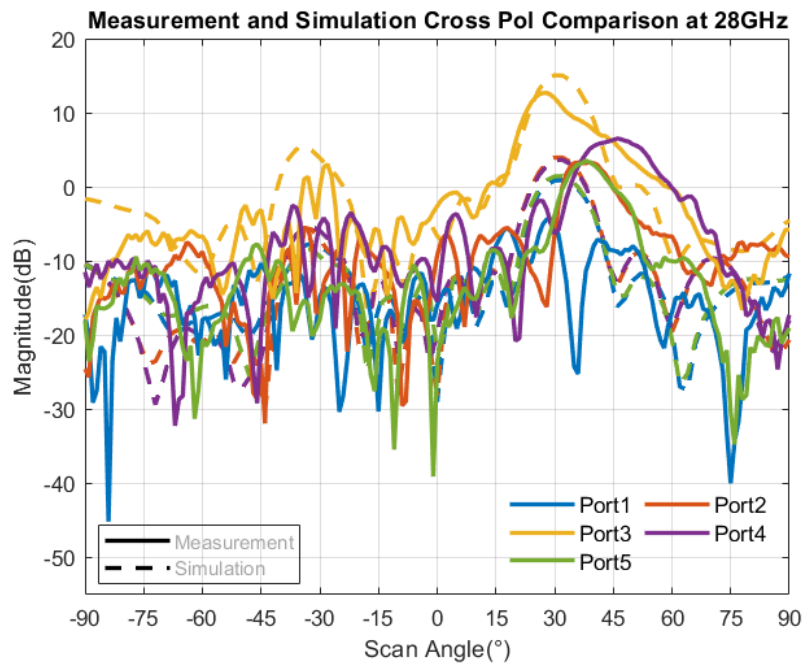


Figure 4.12 Measurement Comparison to Simulation with 0.1mm Air Gap(28GHz)

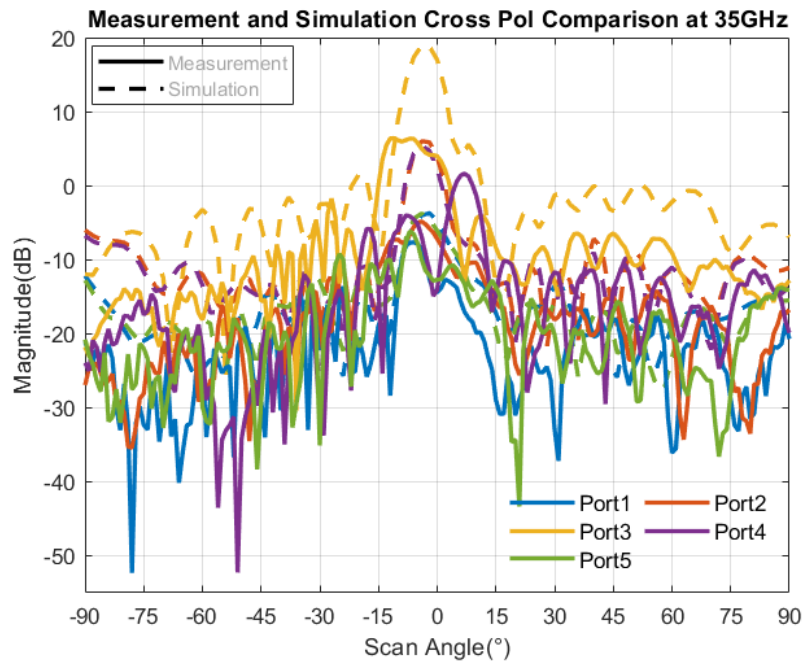


Figure 4.13 Measurement Comparison to Simulation with 0.1mm Air Gap(35GHz)

4.3.3 Epoxy to Hold the Boards Together

To prevent this unwanted interference between the antenna array and the ground layer, the design was assembled again using epoxy on the edges of the two boards. This way, the antenna array could be grounded with as little empty space left between the boards as possible.

Similar to the previous cases, the DUT was taken to the anechoic chamber and the measurements were completed. The measurement results can be seen below in Figure 4.14.

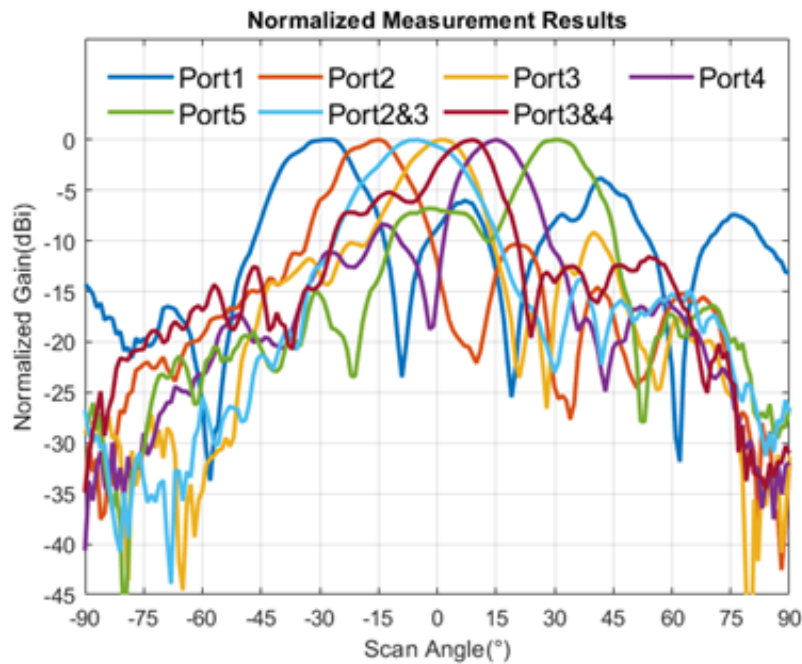


Figure 4.14 Normalized Beams at 31GHz

By assembling the board using the epoxy, the grounding of the array was made better compared to the previous cases. This is evident because of the shapes of the generated beams. In the previous DUT, where only screws were used to hold the boards together, there was an empty space which was about 0.1mm wide. After a shift in center frequency was observed once again, the board was simulated one more time and it was found that there was an air layer left between the ground plane and the array of about 0.03mm wide. The realized gain vs frequency can be seen in Figure 4.15.

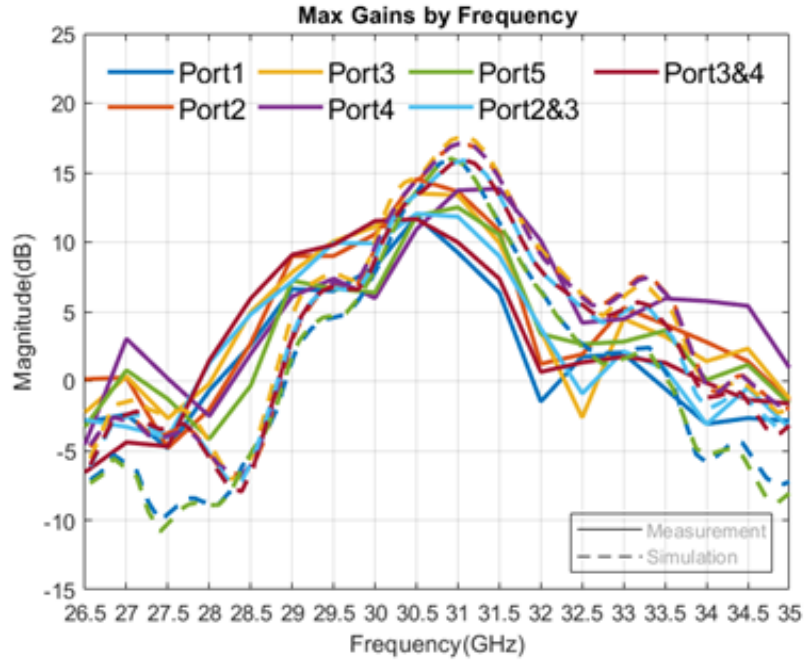


Figure 4.15 Maximum Realized Gain vs Frequency

The measurement results show that the gain values are above 9dBi between 29.5 and 31.5 GHz, making the bandwidth of the design 2GHz. One of the constraints of the Rotman Lens was the 3dB beamwidths of the beams. The beams should have 3dB beamwidths that crossover each other so that changing between the inputs can be smooth. According to the measurements, the design satisfies this condition. From the measurement results, it was observed that the beams cover a space of 80°.

Table 4.1 3dB Beamwidth

Beam Port (Scan Angle)	3dB Beamwidth	
	Simulated (at 28GHz)	Measured (at 31GHz)
Port1 (-27°)	16	19
Port2 (-15°)	16	17
Port2&3 (-5°)	20	23
Port3 (+2°)	16	18
Port3&4 (+9°)	20	15
Port4 (+15°)	16	17
Port5 (+31°)	16	17

Table 4.2 First Sidelobe Level

Beam Port (Scan Angle)	First Sidelobe Level	
	Simulated (at 28GHz)	Measured (at 31GHz)
Port1 (-27°)	-10.7584	-6.01
Port2 (-15°)	-9.8093	-10.3571
Port2&3 (-5°)	-18.1886	-13.8482
Port3 ($+2^\circ$)	-12.7005	-17.137
Port3&4 (-9°)	-18.3668	-5.1995
Port4 ($+15^\circ$)	-9.757	-8.3643
Port5 ($+31^\circ$)	-10.9729	-6.8173

Chapter 5

CONCLUSION

In this thesis, a brief introduction to different types of beamforming networks was covered. Afterwards, the microwave lens was further elaborated on. The Rotman Lens was introduced as a type of microwave lens and some example systems where the Rotman Lens was used were given. Different approaches to the Rotman Lens design were shown, and the design equations of the waveguide Rotman Lens designed by Rotman were derived. After the equations for the waveguide Rotman Lens were derived, they were modified to include the dielectric effects of a substrate, and the equations for the microstrip Rotman Lens were derived.

For this thesis, a microstrip Rotman Lens was designed. The followed design procedure was explained. Each step of the design procedure was shown, and the relevant simulation results were presented. The reflection coefficients and isolations between the ports of the Rotman Lens was presented. Afterwards, the simulation results of the used array were presented. With the array decided, the slot connections between the lens and array were designed. All of the designs were put together and the relevant simulations were completed. After the simulation results of the design were verified, the design was fabricated using low-cost PCB manufacturing techniques. To verify the results obtained from the simulations, the relevant measurements were performed.

Since the design was two layered, different ways to assemble boards together was used. The boards were assembled using glue, screws, and epoxy on the edges of the boards. For all of the different assembly techniques, measurements were done. The results of the measurements were presented. Differences between the initial simulation results and the measurement results were observed. After looking into possible causes of these differences, the cause was found, and new simulations were completed that properly reflect the measured board. The final measurement results

show that the design works between 29GHz and 31.5GHz, with gains over 9dB.

The reason for the initial differences was found to be a layer of air left between the antenna array and the ground layer. After the introduction of this air layer to the simulations, the results were similar to those observed from the measurements. In the future, a way to assemble the boards while also eliminating the air layer can be implemented.

BIBLIOGRAPHY

- [1] R. C. Hansen, *Phased array antennas*. Wiley, 2009.
- [2] S. S. D. Jones, H. Gent, and L. A. A. Browne, “Electromagnetic wave lens and mirror systems.”
- [3] W. Rotman and R. Turner, “Wide-angle microwave lens for line source applications,” *IEEE Transactions on Antennas and Propagation*, vol. 11, no. 6, pp. 623–632, 1963.
- [4] J. Ruze, “Wide-angle metal-plate optics,” *Proceedings of the IRE*, vol. 38, no. 1, pp. 53–59, 1950.
- [5] D. H. Archer, “Radio frequency array antenna employing stacked parallel plate lenses.”
- [6] D. Archer and M. Maybell, “Rotman lens development history at raytheon electronic warfare systems 1967-1995,” in *2005 IEEE Antennas and Propagation Society International Symposium*, vol. 2B, pp. 31–34 vol. 2B, 2005.
- [7] K. Chan, “A feed network for multibeam triangular grid and hexagonal shape planar array antennas,” in *1999 Asia Pacific Microwave Conference. APMC’99. Microwaves Enter the 21st Century. Conference Proceedings (Cat. No.99TH8473)*, vol. 1, pp. 80–83 vol.1, 1999.
- [8] H. Steyskal, C. Cox, and E. Ackerman, “Digital and optical beamforming techniques,” in *IEEE International Symposium on Phased Array Systems and Technology, 2003.*, pp. 616–, 2003.
- [9] S. Clark, C. Martin, V. Kolinko, J. Lovberg, and P. Costianes, “A real-time wide field of view passive millimeter-wave imaging camera,” in *32nd Applied Imagery Pattern Recognition Workshop, 2003. Proceedings.*, pp. 250–254, 2003.
- [10] S. Vashist, M. K. Soni, and P. K. Singhal, “A review on the development of rotman lens antenna,” *Chinese Journal of Engineering*, vol. 2014, p. 1–9, 2014.

- [11] J. Shelton, "Focusing characteristics of symmetrically configured bootlace lenses," *IEEE Transactions on Antennas and Propagation*, vol. 26, no. 4, pp. 513–518, 1978.
- [12] T. Katagi, S. Mano, and S. Sato, "An improved design method of rotman lens antennas," *IEEE Transactions on Antennas and Propagation*, vol. 32, no. 5, pp. 524–527, 1984.
- [13] D. Gagnon, "Procedure for correct refocusing of the rotman lens according to snell's law," *IEEE Transactions on Antennas and Propagation*, vol. 37, no. 3, pp. 390–392, 1989.
- [14] R. Hansen, "Design trades for rotman lenses," *IEEE Transactions on Antennas and Propagation*, vol. 39, no. 4, pp. 464–472, 1991.
- [15] J. Dong, *Microwave lens designs: Optimization, fast simulation algorithms, and 360-degree scanning techniques*. PhD thesis, 2009.
- [16] E. H. Mujammami, I. Afifi, and A. B. Sebak, "Optimum wideband high gain analog beamforming network for 5g applications," *IEEE Access*, vol. 7, pp. 52226–52237, 2019.
- [17] M. R. Naeini and M. Fakharzadeh, "A 28 ghz beam-switching yagi-uda array using rotman lens for 5g wireless communications," in *2017 IEEE International Symposium on Antennas and Propagation USNC/URSI National Radio Science Meeting*, pp. 2617–2618, 2017.
- [18] M. Heino, C. Icheln, J. Haarla, and K. Haneda, "Pcb-based design of a beam-steerable array with high-gain antennas and a rotman lens at 28 ghz," *IEEE Antennas and Wireless Propagation Letters*, vol. 19, no. 10, pp. 1754–1758, 2020.
- [19] A. M. A. Najafabadi, F. A. Ghani, and I. Tekin, "A 28 ghz beam steerable elliptic microstrip array antenna for 5g applications," in *2022 16th European Conference on Antennas and Propagation (EuCAP)*, pp. 1–4, 2022.
- [20] W. Lee, J. Kim, and Y. J. Yoon, "Compact two-layer rotman lens-fed microstrip antenna array at 24 ghz," *IEEE Transactions on Antennas and Propagation*, vol. 59, no. 2, pp. 460–466, 2011.